國立臺灣大學理學院地理環境資源學系

學士班學生論文

Department of Geography

College of Science

National Taiwan University

Bachelor's Thesis

估計2018年花蓮地震離斷層變形側向變化

Estimating along-strike variation of off-fault deformation for the 2018 Mw 6.4 Hualien Earthquake

李旻

Min Lee

指導教授：莊昀叡 博士

Advisor: Ray Y. Chuang, Ph.D.

中華民國112年4月

April, 2023

摘要

地表變形的評估是了解斷層活動以及減災的重要項目之一，目前近斷層的變形主要是透過現地測量計算位移量，而區域性的同震地表位移則仰賴測地學的工具以推估整體的地表變形場。然而，斷層活動可以造成離斷層線幾十公里外的非彈性變形，稱為離斷層變形（off-fault deformation），是現地測量難以偵測到的地表變動。由於離斷層變形量會可能會影響地震災害與潛勢的評估，近年來隨著測量的技術進步，各個主要地震離斷層變形的量化，以及造成變形的特性逐漸受到重視。

2018年發生於台灣東部的花蓮地震，地震矩規模高達6.4，是近年台灣地區重要的災害地震之一。根據前人研究，現地調查顯示地表破裂在米崙斷層北段較為集中，而在南段進到市區之後則分散為多條破裂；而透過全球衛星導航系統(GNSS)、合成孔徑雷達(SAR) 與光學衛星影像，區域的地表位移量也有從北往南減小的趨勢，顯示米崙斷層應有明顯的離斷層變形側向變化。但由於現地調查只侷限於地表破裂上，衛星觀測則提供遠場（far-field）觀測而於近場（near-field）無精確的觀測，所以目前並未有離斷層變形側向變化的量化估計。因此，本研究針對2018年花蓮地震，利用運動恢復結構技術（structure from motion）於震前與震後的航空影像，產生高解析度的正射影像，並利用次像素關聯法計算近場位移量，搭配前人研究的遠場觀測與地表破裂資料，計算離斷層變形的佔比與側向變化。研究結果顯示米崙斷層上下盤的平均南北向位移差值為1.56公尺，平均東西向位移差值為1.10公尺。沿著位移落差的位置可以準確繪製出斷層線，本研究所繪製出的斷層線較前人研究更稍偏向東側。位移場的結果顯示了沿米崙斷層明顯的左移破裂，在斷層中段的地表破裂較為集中，變形範圍也較為狹窄；到了南段，地表變形區變得更寬（300公尺）、更分散。本研究也計算了離斷層變形的沿走向變化，發現離斷層變形的百分比在中段相對較低（~68%），但有向南增加的趨勢（~97%）。

關鍵字：離斷層變形、2018 花蓮地震、近場破裂帶、運動回復結構、干涉合成孔徑雷達

Abstract

The assessment of surface deformation is one of the important aspects for understanding fault activity and disaster mitigation. Currently, near-fault deformation is mainly calculated by in situ measurements, while regional coseismic surface displacement relies on geodetic tools to estimate the overall surface deformation field. However, fault activity can cause inelastic deformation tens of kilometers away from the fault line. This is called off-fault deformation, a difficult surface change to be detected by in situ measurements. Since the amount of off-fault deformation may affect the assessment of earthquake hazard and potential, the quantification of off-fault deformation of major earthquakes and the characteristics of the resulting deformation have received increasing attention in recent years with the advancement of measurement technology.

The Hualien earthquake occurred in eastern Taiwan in 2018 with a moment magnitude of 6.4 and was one of the most important catastrophic earthquakes in Taiwan in recent years. According to previous studies, the surface rupture was more concentrated in the northern part of the Milun fault, while the southern part was scattered into multiple ruptures after entering the urban area. And through GNSS, synthetic aperture radar and optical satellite images, the surface displacement of the region also tended to decrease from north to south, indicating that the Milun fault should have obvious lateral changes of off-fault deformation. However, because the in situ investigation is only limited to surface rupture, and satellite observation provides far-field observation without precise observation in near-field, there is no quantitative estimation of the lateral change of off-fault deformation. Therefore, in this study, the

structure from motion technique was used to generate high-resolution orthophotos from pre- and post-earthquake aerial images of the 2018 Hualien earthquake, and the sub-pixel correlation method was used to calculate the near-field displacements, together with the far-field observations and surface rupture data from previous studies, to calculate the proportional and lateral changes of the off-fault deformation. The results show that the average N-S displacement difference between the upper and lower part of the Milun fault is 1.56 m, and the average E-W displacement difference is 1.10 m. The fault line can be accurately mapped along the position of the displacement drop, and the fault line mapped in this study is slightly more to the east than previous studies. The displacement field show a clear leftward rupture along the fault, with more concentrated surface rupture and narrower deformation in the middle part of the fault, and a wider (300 m) and more dispersed surface deformation zone in the southern part. In this study, we also calculated the along-strike variation of off-fault deformation and found that the percentage of off-fault deformation is relatively low in the middle section (~68%), but tends to increase southward (~97%).

Keywords: Off-fault deformation, 2018 Hualien earthquake, Near-field rupture zone, Structure from Motion, InSAR

Acknowledgement

I would like to thank my advisor Dr. Ray Y. Chuang who has always been supportive and open to many questions including both academic and life. I also want to thank my committee Dr. Yu-Ting, Kuo and Dr. Ling-Ho, Chung for all the critical suggestions that help complete this study.

I also owe lots of gratitude to all the 303 lab members who are always there for me. The time we shared together was priceless and the help was immense. I wish the best of us in the following years when we will be pursuing our life goals and achievements. Lastly, I want to show my biggest love and appreciation to my parents, Mike and Eva, and my little brother, James. I have been raised in a caring family that has always been the strongest support. I received the love that one can ever ask for and words can hardly describe. Nothing of these could be possible if it weren't for you.

Table of Contents

List of Figures

List of Tables

Chapter 1 Introduction

1.1 Motivation

How Earth's surface deforms during earthquakes is crucial for understanding active structures and earthquake physics. As field investigations are generally limited to the area along fault lines and surface ruptures, which have discernible offsets, geodetic approaches can detect subtle deformation at a larger spatial scale. In addition to surface ruptures, coseismic surface deformation has varied types including secondary faulting and distributed deformation such as warping, distributed granular flow, and rotation that occurs outside of the surface rupture. The distributed deformation may be significantly large compared to the deformation along surface ruptures, leading to the research topic of off-deformation. Instead of being close to surface ruptures, off-fault deformation could be distributed within tens of kilometers away from the fault lines and sometimes higher than half of the total deformation (e.g. Zinke et al., 2014). With accurate assessments of off-fault deformation, ones can better estimate fault behaviors and evaluate disaster mitigation by mapping geologically sensitive area.

With the development of geodetic approaches nowadays, geodetic observations at the coseismic period have higher spatial resolution and spatial coverage, drawing attention to the presence of off-fault deformation. In order to quantify off-fault deformation, surface-displacement profiles derived from geodetic methods can help constrain the amount of far-field, off-fault deformation (Zinke et al., 2014; Milliner et al., 2015). The geodetic observations provide insights into the localization of fault slip and inelastic strain (Barnhart et al., 2020). Since several geodetic techniques like GNSS,

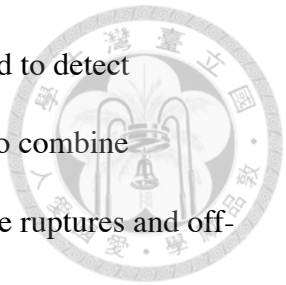

InSAR, and offset tracking of remote sensing imagery are widely used to detect coseismic deformation nowadays, it is important to understand how to combine different geodetic data and further characterize comprehensive surface ruptures and off-fault deformation.

In recent years, the 2018 Mw6.4 Hualien earthquake is one of the most hazardous seismic event, causing several casualties and building collapse. The characteristics of the movement of the Milun fault is important to understand the tectonic at the northernmost Longitudinal Valley and the interaction between the Central Range fault and Longitudinal Valley fault system (Shyu et al., 2016; Yen et al., 2019). Geodetic observations show that the coseismic displacements of the Hualien earthquake maximizes toward the northern end of the Milun fault and decreases to the south (Kuo et al., 2019; Yen et al., 2019). Similarly, surface ruptures are localized toward the north and become more distributed to the south (Huang et al., 2019; Lin et al., 2019). The Hualien earthquake has long wavelength deformation could be induced by the buried main rupture front beneath the surface, with inelastic off-fault deformation very close to the surface (Kuo et al., 2019). With the basic understanding of the pattern of the coseismic deformation, however, the amount of the along-strike variation of the off-fault deformation is less constrained. Therefore, this research aims to combine varied geodetic data to better estimate the along-strike variation of the off-fault deformation for the Hualien earthquake.

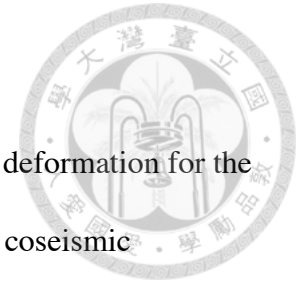

1.2 Research purpose

In order to quantify the along-strike variation of the off-fault deformation for the 2018 Hualien earthquake, it requires comprehensive observations of coseismic deformation at local and regional scales. While ground investigation (Huang et al., 2019; Hsu et al., 2019; Lin et al., 2019) and satellite imagery and GNSS (Huang et al., 2018; Kuo et al., 2019; Yen et al., 2019; Wu et al., 2019) have covered the on-fault and far-field observations, respectively, the near-field observations in between, which is the key to understand the amount of off-fault deformation, requires observations with fine spatial coverage and resolution. Aerial images, which have higher spatial resolution (~50 cm) than satellite images, should provide suitable observations for the near-field deformation. Since GNSS, InSAR, and field investigation data are already accessible, the goal of this research is to process aerial imagery before and after the 2018 Hualien earthquake to complete full surface observations of the earthquake. With the constraints from other data, the estimation of off-fault deformation show clear horizontal deformation field across the Milun fault and provides an opportunity to quantitatively evaluate the along-strike variation of the off-fault deformation and to explore the controlling factors of the variation.

Chapter 2 Literature review

2.1 Hualien earthquake

The 2018/02/06 Mw 6.4 Hualien earthquake struck the nearshore Hualien at 23:50 local time with a shallow hypocenter depth of about 6.3 km, causing a high seismic intensity of 7 in Hualien City. The earthquake generated surface ruptures along the Milun fault and the northern most part of the Lingding Fault (CWB, 2018). This earthquake was accompanied by one foreshock and many aftershocks with magnitude larger than 5 (Fig. 1). The aftershock sequence showed a tendency of clustering over a northeast-striking structure extending towards on-land with mostly normal faulting mechanisms on a steep west-dipping nodal plane (Kuo-Chen et al., 2019).

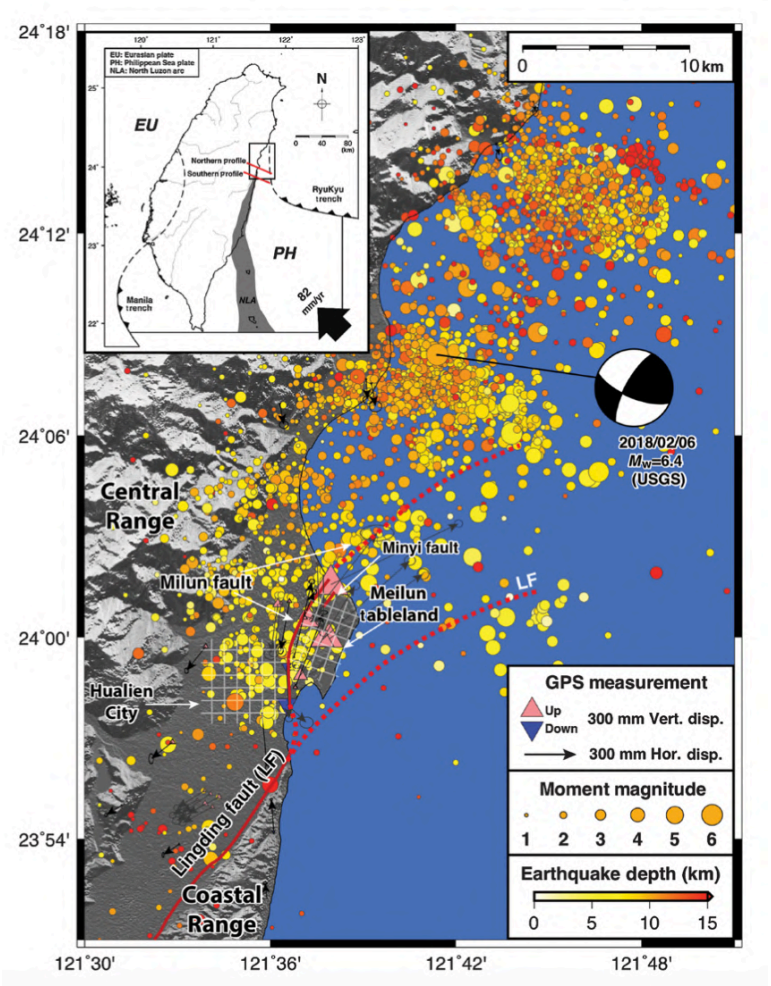

Fig. 1. Focal mechanism and moment magnitudes of the 2018 Hualien earthquake. The South China Sea (Eurasian plate) is subducting eastward beneath the Philippine Sea plate along the Manila trench south of Taiwan, and the Philippine Sea plate is subducting northward beneath the Eurasian plate. Crustal blocks east of both faults move north relative to central Taiwan via left-lateral fault offset; the relative motion becomes more eastward because of local clockwise rotation near the north end of the Milun fault. (Yen et al., 2019)

The major surface ruptures could be categorized into synthetic and antithetic Riedel shears interlinked by push-up moletracks or tensional fissures (Huang et al., 2019; Lin et al., 2019). The strike of the principal displacement zone evolved from northeast to northwest. Lee et al. (2019) suggested that the rupture started from the west-dipping fault plane in the north and propagated to the south, triggering the slip on the Milun Fault and then the Lingding Fault based on the results of joint source inversion. Yang et al. (2018) proposed that the ruptures of the Milun Fault and an unknown west-dipping fault were triggered by a west-dipping seismogenic fault from the north with the faulting models using InSAR and GNSS results. A general interpretation for the different results from different models is that the slip on the Milun Fault was triggered from the seismogenic fault in the north and propagated towards the south.

2.2 Study area

2.2.1 Study area

The study area for this research is basically along the Milun Fault. The exact frame for the study area is from 121.551E to 121.701E, and from 23.951N to 24.051N (WGS 84). The frame is slightly wider than previous researches due to that we aims to study off-fault deformation which could cross the areas from near field to far field.

2.2.2 Milun fault

The ruptures along Milun fault include a maximum left-lateral offset of ~77 cm, at the northern tip of the Milun tableland (Huang et al., 2019). The mapped surface ruptures generated significantly less surface displacement in the city, with an average measurable left-lateral offset of ~15 cm across the damage zone along the southern half of the Milun fault (Huang et al., 2019; Lin et al., 2019) (Fig. 2).

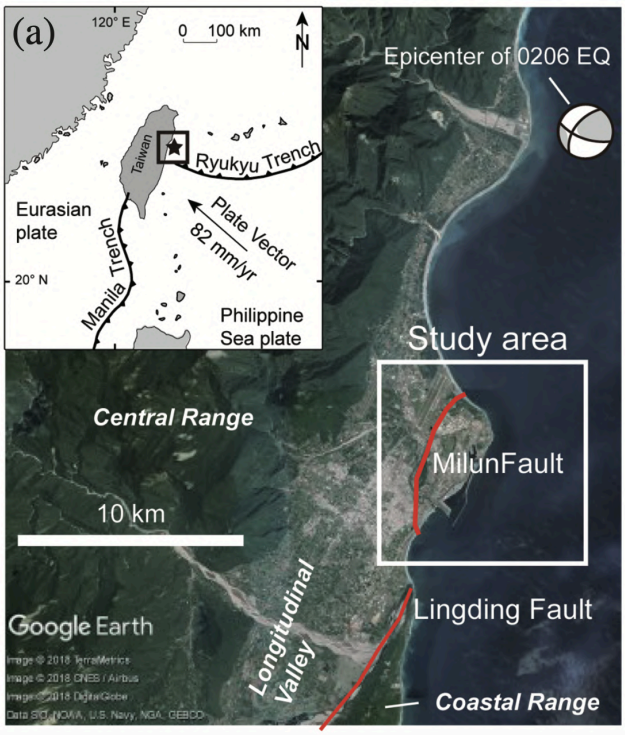

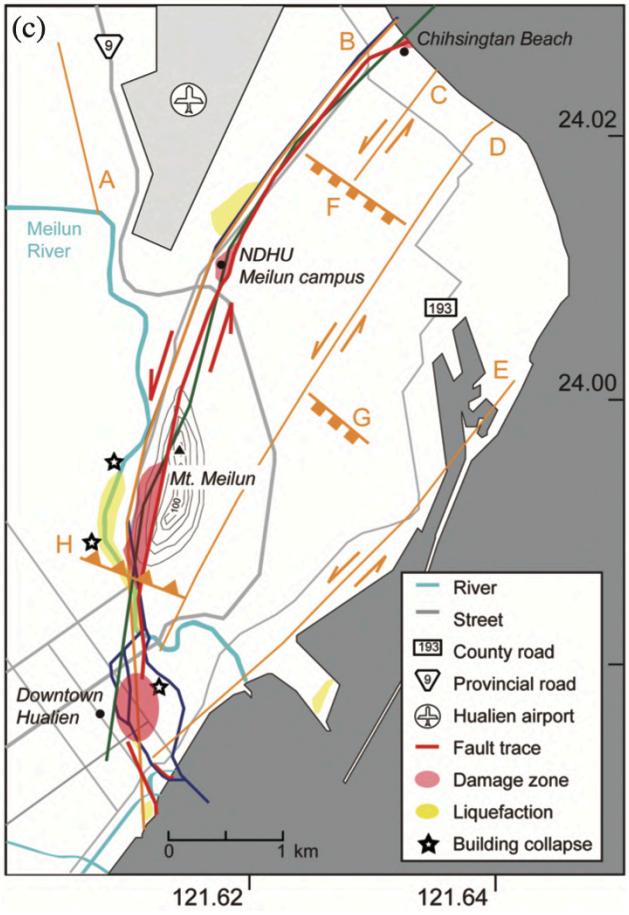

Fig. 2. Map of faults and surface ruptures. (a) The regional map of the study area. (c) Schematic map of the 2018 fault trace and the surrounding structures. (Huang et al., 2018)

The Milun Fault is considered as a Holocene active fault due to the reason that it is the only earthquake fault with documented fault displacement of the 1951 Hualien-Taitung earthquake sequence (Yang, 1953; Hsu, 1962; Bonilla, 1975, 1977; Cheng et al., 1999; Shyu et al., 2005). The earthquake sequence includes three magnitude 7 events on the north end of the Longitudinal Valley on 22 October and two magnitude 6 earthquakes on 25 November. The exact locations of the 1951 fault ruptures are still ambiguous due to the absence of coordinate records. With the photos only showing massive toppling and collapse of houses rather than validated surface ruptures, it is more questionable how the segments connected to each other. The possible solution is

that the proposed fault segments may only represent the envelope area of the damage zone.

2.2.3 Surrounding geologic structures

Structures around the Milun Fault include the northeast-striking strike-slip faults of the Minyi Fault (Lin and Hsiao, 1998; CGS, 2010; Yen et al., 2011) and the Nanbin Fault (Lin and Hsiao, 1998); the northwest-striking normal faults of the Chihsingtan Fault (Lin and Hsiao, 1998) and the East Minyi Fault (Lin and Hsiao, 1998; Chen et al., 2014); the northwest-striking topographic high of the Beipu structure (Chen et al., 2014); and to the southeast, the Lingding Fault which bounds the western side of the Coastal Range (CGS, 2010).

Chapter 3 Data and methods

3.1 Data

3.1.1 Aerial images

Aerial image from Aerial Survey Office, Forestry Bureau, Council of Agriculture were the data for generating orthoimages. The range of the photographs started from August 23, 2016 to March 4, 2018, including the date of Hualien earthquake. The flight strips in 2016 are 160823e_64, 160827b_63, 160827b_64, 160827b_65 and 160827b_66. As for in 2018, the flight strips are 180304b_64, 180304b_65 and 180304b_66 (Table 1).

2016/08/23	2016/10/27		2018/03/04	
160823e-160823e_64_0103	161027b-161027b_63_0003	161027b-161027b_65_0033	180304b-180304b_64_0048	180304b-180304b_65_0018
160823e-160823e_64_0104	161027b-161027b_63_0004	161027b-161027b_65_0034	180304b-180304b_64_0049	180304b-180304b_65_0019
160823e-160823e_64_0105	161027b-161027b_63_0005	161027b-161027b_65_0035	180304b-180304b_64_0050	180304b-180304b_65_0020
160823e-160823e_64_0106	161027b-161027b_63_0006	161027b-161027b_65_0036	180304b-180304b_64_0051	180304b-180304b_65_0021
160823e-160823e_64_0107	161027b-161027b_63_0007	161027b-161027b_65_0037	180304b-180304b_64_0052	180304b-180304b_65_0022
160823e-160823e_64_0108	161027b-161027b_64_0054	161027b-161027b_65_0038	180304b-180304b_64_0053	180304b-180304b_65_0023
160823e-160823e_64_0109	161027b-161027b_64_0055	161027b-161027b_65_0039	180304b-180304b_64_0054	180304b-180304b_65_0024
160823e-160823e_64_0110	161027b-161027b_64_0056	161027b-161027b_65_0040	180304b-180304b_64_0055	180304b-180304b_65_0025
160823e-160823e_64_0111	161027b-161027b_64_0057	161027b-161027b_65_0041	180304b-180304b_64_0056	180304b-180304b_66_0044
	161027b-161027b_64_0058	161027b-161027b_65_0042	180304b-180304b_64_0057	180304b-180304b_66_0045
	161027b-161027b_64_0059	161027b-161027b_65_0043	180304b-180304b_64_0058	180304b-180304b_66_0046
	161027b-161027b_64_0060	161027b-161027b_65_0044	180304b-180304b_64_0059	
	161027b-161027b_64_0061	161027b-161027b_65_0045	180304b-180304b_64_0060	
	161027b-161027b_64_0062	161027b-161027b_66_0077	180304b-180304b_64_0061	
	161027b-161027b_64_0063	161027b-161027b_66_0078	180304b-180304b_65_0008	
	161027b-161027b_64_0064	161027b-161027b_66_0079	180304b-180304b_65_0009	
	161027b-161027b_64_0065	161027b-161027b_66_0080	180304b-180304b_65_0010	
	161027b-161027b_64_0066	161027b-161027b_66_0081	180304b-180304b_65_0011	
	161027b-161027b_64_0067	161027b-161027b_66_0082	180304b-180304b_65_0012	
	161027b-161027b_65_0028	161027b-161027b_66_0083	180304b-180304b_65_0013	
	161027b-161027b_65_0029	161027b-161027b_66_0084	180304b-180304b_65_0014	
	161027b-161027b_65_0030	161027b-161027b_66_0085	180304b-180304b_65_0015	
	161027b-161027b_65_0031	161027b-161027b_66_0086	180304b-180304b_65_0016	
	161027b-161027b_65_0032	161027b-161027b_66_0087	180304b-180304b_65_0017	

Table 1. List of aerial photos used in this research with dates and numbers.

Aerial images in 2018 are partially covered by clouds, therefore the set along the coastline wouldn't be selected for further processing. The color has been automatically adjusted twice by Photoshop before any process in Metashape. We have tested four sets of aerial photos with different resolution, from 5000*5000 to 12000*12000, and for the final result we have chosen 7680*13820 to process and present.

3.1.2 Coseismic displacements from GNSS and satellite data

Yen et al. (2019) estimated 3D surface displacements by using GNSS, InSAR, and pixel offsets for intensity images. Yen et al. (2018) used GMTSAR software (Sandwell et al., 2011) for InSAR processing, including respective removal of orbit ramp and topographic phase by precise orbit from ESA and ALOS 15 m digital elevation model. SNAPHU software was used for unwrapping interferograms to the LOS displacement field (Chen and Zebker, 2002). Lin (2022) also proposed three versions of 3D displacement fields were proposed and the best one among all was Version 3 which was inverted from DInSAR and fusion of Pixel-offset Tracking (POT) and Multiple Aperture Interferometry (MAI) based on spatial resolution, accuracy and deformation patterns. Kuo et al. (2019) used optical satellite images to compute horizontal displacements. This study used 3D surface displacements from Yen et al. (2019) to constrain far-field deformation and use horizontal near-field displacements from Kuo et al. (2019) to verify the surface displacements derived from aerial images generated in this study.

3.1.3 Surface rupture data

This study used surface rupture data from the mapping results of field investigations (Huang et al., 2019 and Hsu et al., 2019) and UAV surveys (Lin et al., 2019). UAV images provide detailed surface deformation along the fault line with much higher resolution than satellite image. The resolution of our UAV photos can reach higher than 10 cm, presenting a fine 3-D surface model with SfM technique.

3.2 Methods

Our methods could be divided into two steps. The first step is to process aerial photos and produce raw COSI-Corr displacement field. The next step is correcting our COSI-Corr result with GNSS coseismic deformation data and estimating the variation of off-fault deformation from north to south (Fig. 3).

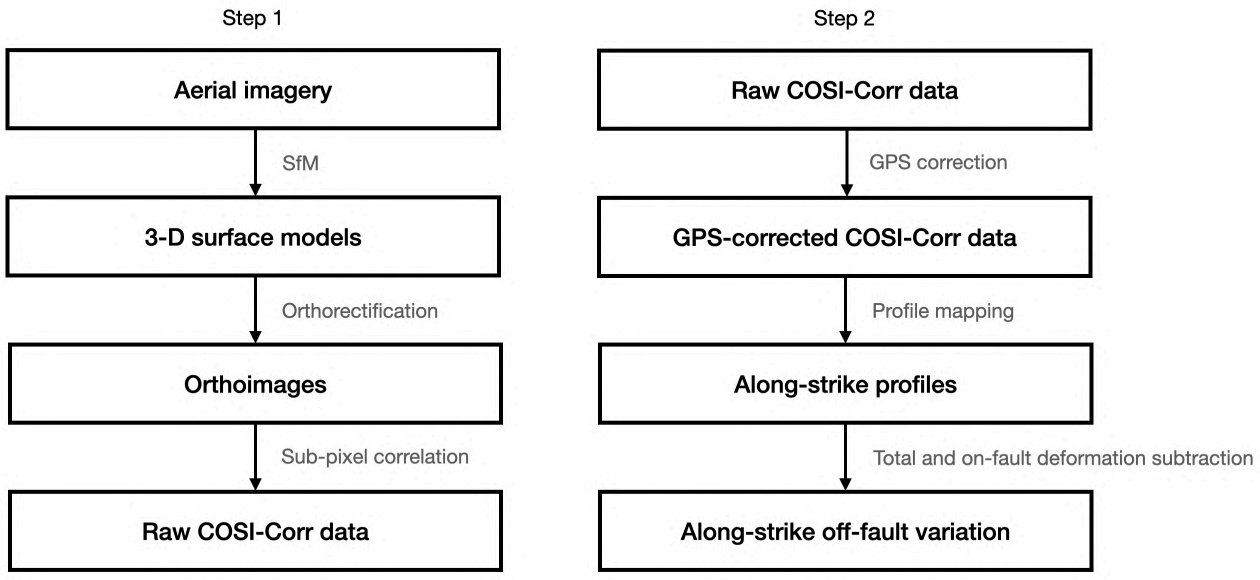

Fig. 3. Flow chart of research process.

3.2.1 Aerial image processing

3.2.1.1 3D model and orthoimage from SfM

Structure from motion (SfM) is the process of estimating the 3-D structure of a scene from a set of 2-D images. This research built the 3-D terrain model with Metashape software. We loaded a series of aerial images into Metashape and aligned them. 58 and 34 photos in 2016 and 2018 were successfully aligned. To provide these images with coordinates, we have chosen two sets of ground control points before and after the earthquakes.

Ground control points are chosen from the 2010 TWD97 orthoimage by the National Land Surveying and Mapping Center. The set before the earthquake has 67 points, and the other has 56 points, covering the whole research area except for the airport and other defense land (Fig. 4). The airport and the defense land have been mosaicked by the government, therefore showing all black on our orthoimages.

The set of ground control points after the earthquake include another set of ground control points measured right after the earthquake, which is called 2010A. Two 2010A control points were in the research area, which are HUAL and PEPU. With these new control points, specifically measured for the ground change from the earthquake, the results in COSI-Corr will have better accuracy. About half of the ground control points were later chosen as check points, which were basically in the middle for validation. The final precision by adjusting control and check points is 0.27 meter and 0.29 meter.

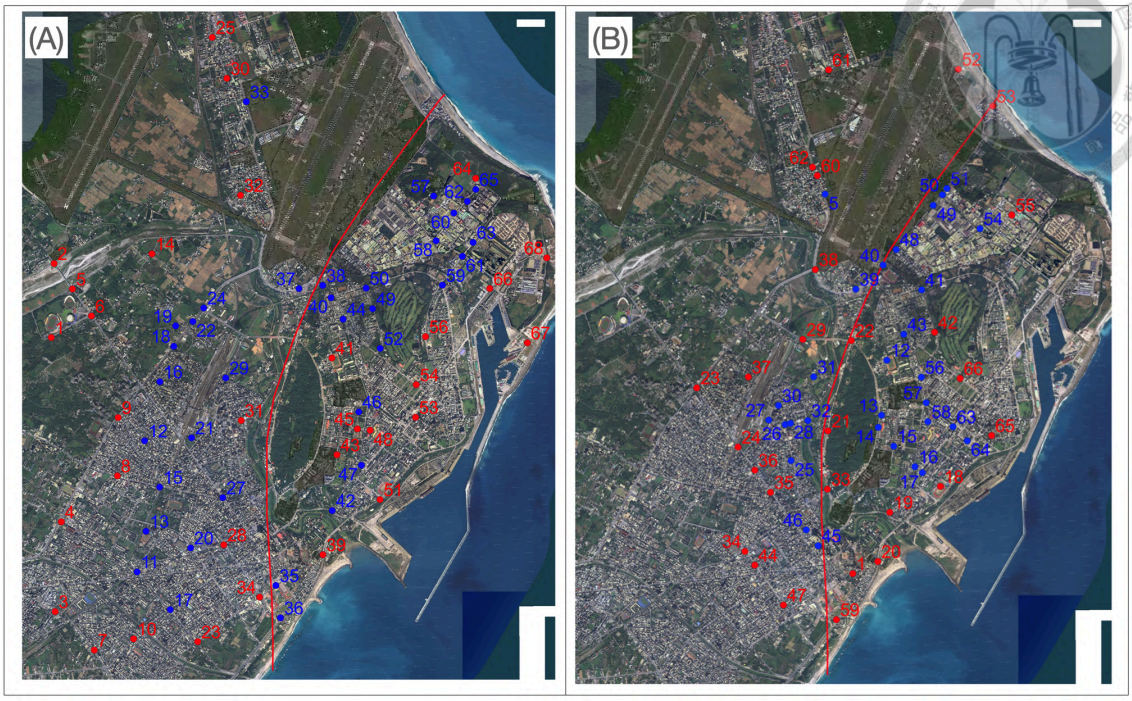

Fig. 4. Ground control points before and after the 2018 Hualien earthquake. Red dots are control points; blue dots are check points. (A) 2016 ground control points. (B) 2018 ground control points were limited to the city area due to the lack of aerial photos in the mountains and along the coastline.

Dense clouds were built with 308,712,858 and 209,126,988 points in high quality, disabled filtering. After the dense cloud were built, we built mesh and texture with 94,527,466 and 64,846,647 faces in high quality for the final step, generating orthoimages and DSM (Figs. 5 and 6). The size of orthoimage is 39326*51216 and 26812*48467 with pixel size of 29.5 and 27.3 cm. The errors are shown below in Table 2.

	Control points error (m)	Control points error (pix)	Check points error (m)	Check points error (pix)
2016	0.767588	0.279	0.947686	0.147
2018	3.899569	1.672	7.766680	0.248

Table 2. Control point errors and check point errors in 2016 and 2018. The control point and check point errors were significantly bigger than those in 2016 due to the quality of the original imagery from the Forestry Bureau. The 6500*6500 set also showed a similar result.

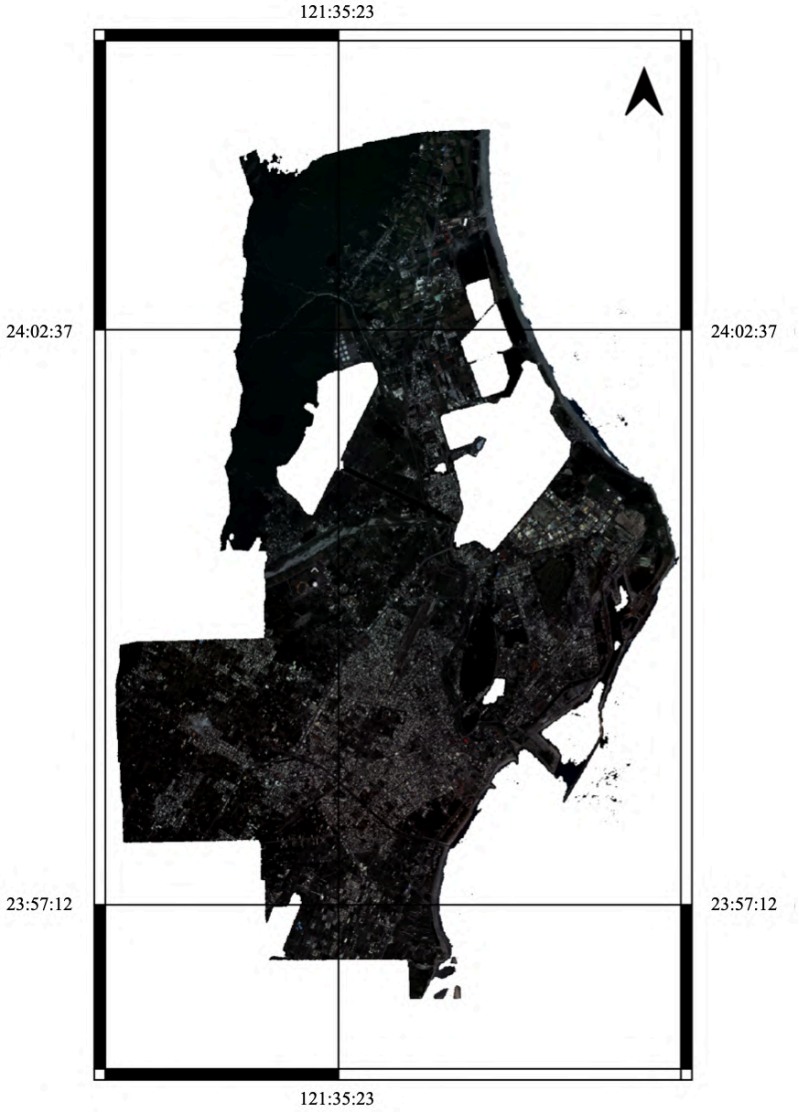

Fig. 5. 2016 Orthoimage before the earthquake.

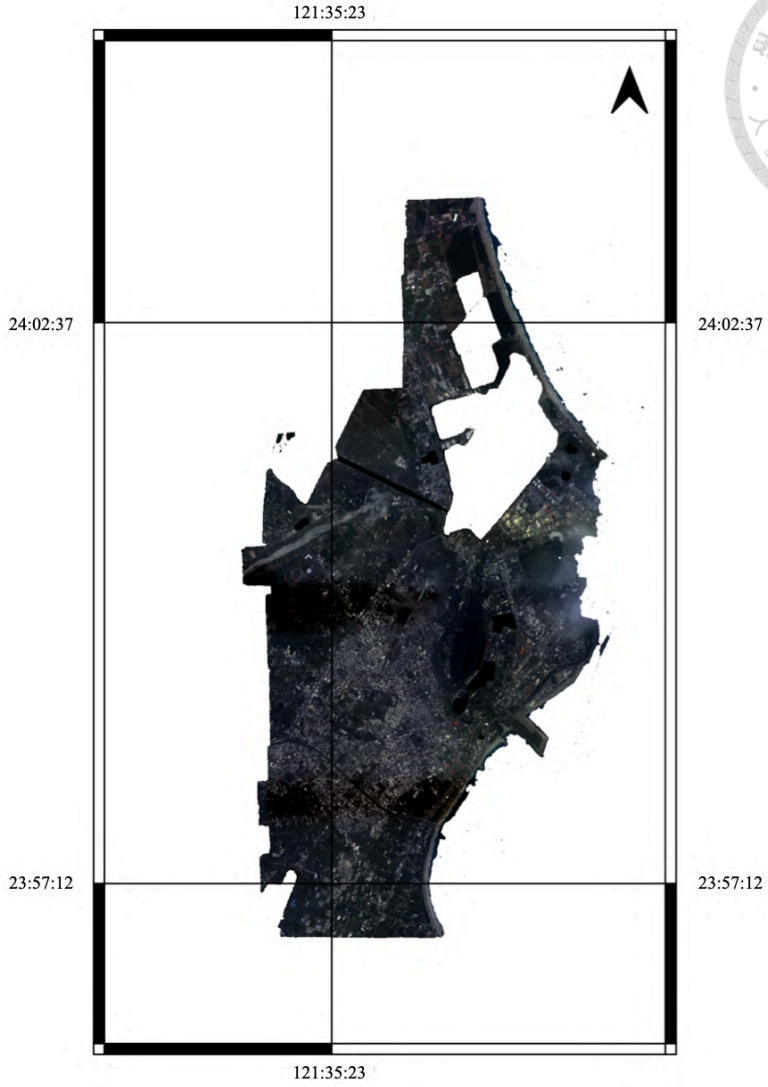

Fig. 6. 2018 Orthoimage after the earthquake. Orthoimage in 2018 had lower coverage of the mountain and coastline area due to high cloud coverage, non-ideal weather condition and the lack of aerial images.

3.2.1.2 COSI-Corr by ENVI

COSI-Corr (Coregistration of Optically Sensed Images and Correlation) is a software developed at the California Institute of Technology for the accurate geometrical processing of optical satellite and aerial imagery. The software allows precise co-registration of time-series of images and sub-pixel measurement of ground

surface deformation. By comparing the two optical images before and after the earthquake, we can see where each pixel (or window) was moved after the earthquake, calculate its displacement value, and finally obtain the coseismic displacement field of the whole area. This method was applied on the calculation of horizontal displacement.

However, if only pixels are used as the calculation unit, the calculated displacement will be a multiple of the pixel size. To enhance the precision of displacement, we need to obtain the pixel-to-pixel information around the location with the strongest linear correlation by using spectral data and image interpolation. This way, the distance of ground change can be calculated smaller than the size of the pixels. In short, it can detect displacement with an accuracy of 1/10 to 1/20 times the image resolution (Van Puymbroeck et al., 2000). The maximum offset (77 cm) is suitable for aerial images with a resolution of 0.5 meter using sub-pixel correlation, where displacement range of 2.5 to 5 centimeters can be detected.

Before put into COSI-Corr, the orthoimages before and after the earthquake need to have the exact same frame size and pixel size. Therefore, we resampled the two gray images with the new pixel size of 0.3 meter in Nearest way (Fig. 7).

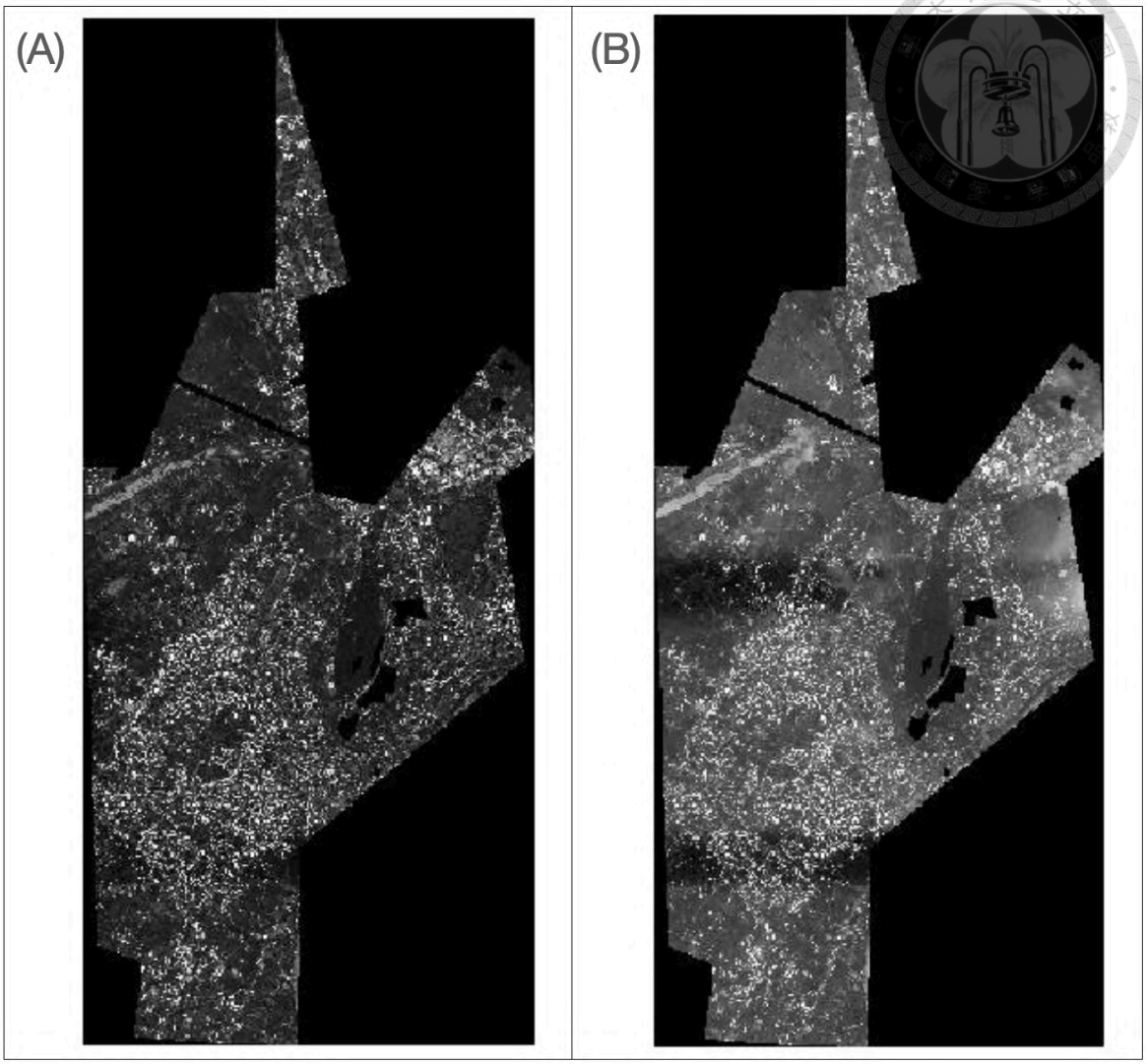

Fig. 7. Resampled and clipped gray images in 2016 (A) and 2018 (B).

In order to remove noise or extreme values to make the result smoother, we do a Fourier Transform on the images in a moving window (Van Puymbroeck et al., 2000). The size of the window would affect the sharpness of the data; the larger the window, the smoother the result. Then, we had to decide how many pixels we need to do one window Fourier transformation. The interval size would determine its resolution; the larger the interval, the worse the resolution. In addition, the window size should be bigger than the interval, so that some pixels wouldn't be left out of the calculation (Fig.

8). Finally, the results are compared for correlation and the position with the strongest linear correlation is the relative displacement of that point.

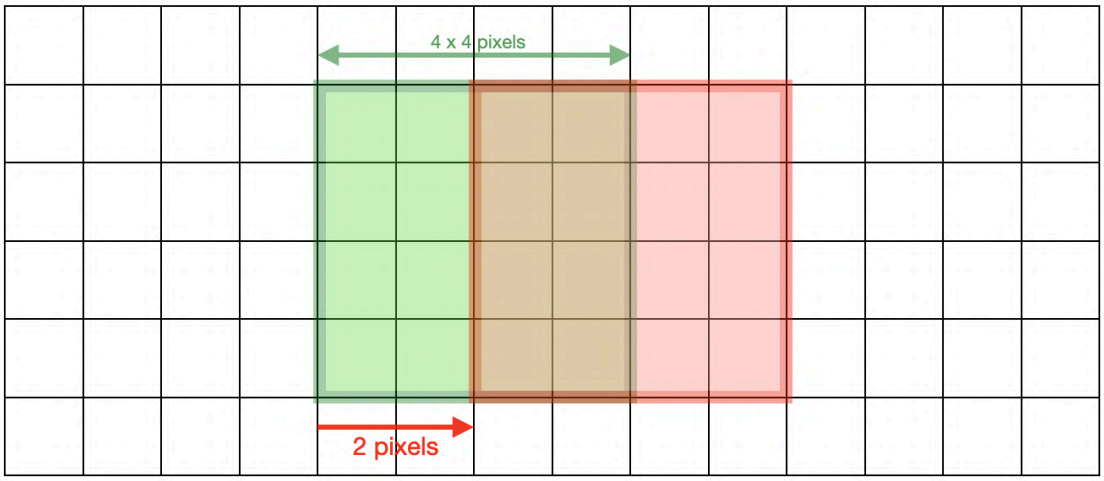

Fig. 8. Fourier Transform in a moving window. The window size is 8x8 pixels with 2 pixels interval.

The correlation masking threshold can help us to exclude the points with low correlation during the comparison. When there are house collapses, landslides, or cloud cover in the images, these points will not correspond and the correlation is very low and should be excluded (Dominguez et al., 2003). The threshold for this research is set as 0.9, which is the optimal value based on the result we tested on the 921 earthquake.

Different combinations of parameters would produce different results. Although a larger moving window can help us to exclude extreme values, excessive smoothing could lost some specific points. Therefore, we must different sets of parameters to find the most suitable combination. Table 3. Shows all the parameter combination we have tested. According to our experience, the COSI-Corr results are usually the best when the window size X and Y is four times larger than the step X and Y. The best parameters we

have tried for a clear COSI-Corr result are 128*128 pixels for window size and 32 pixels for step.

	Window size X*Y (pixel)					
Step (pixel)	4*4	8*8	16*16	32*32	64*64	128*128
2		X	X			
4			X	X		
8				X	X	X
16				X	X	X
32					X	V
64						X

Table 3. Parameter combinations for COSI-Corr. The window size should be bigger than the step (interval), so that some pixels wouldn't be left out of the calculation. The red zone excluded the parameter combinations that are not ideal to use from the table. X means the combination we have tested; V means the optimal pair.

The horizontal displacement in E-W direction is insignificant, which is consistent with previous researches from Huang et al. (2019), Kuo et al. (2019) and Yen et al. (2019). The initial result from COSI-Corr showed maximum 140 centimeters of N-S left-lateral offset between two walls, which is a little bigger then the result from Huang et al. (2019), indicating left-lateral offset of ~77 cm at the northern tip of the Milun tableland (Fig. 9).

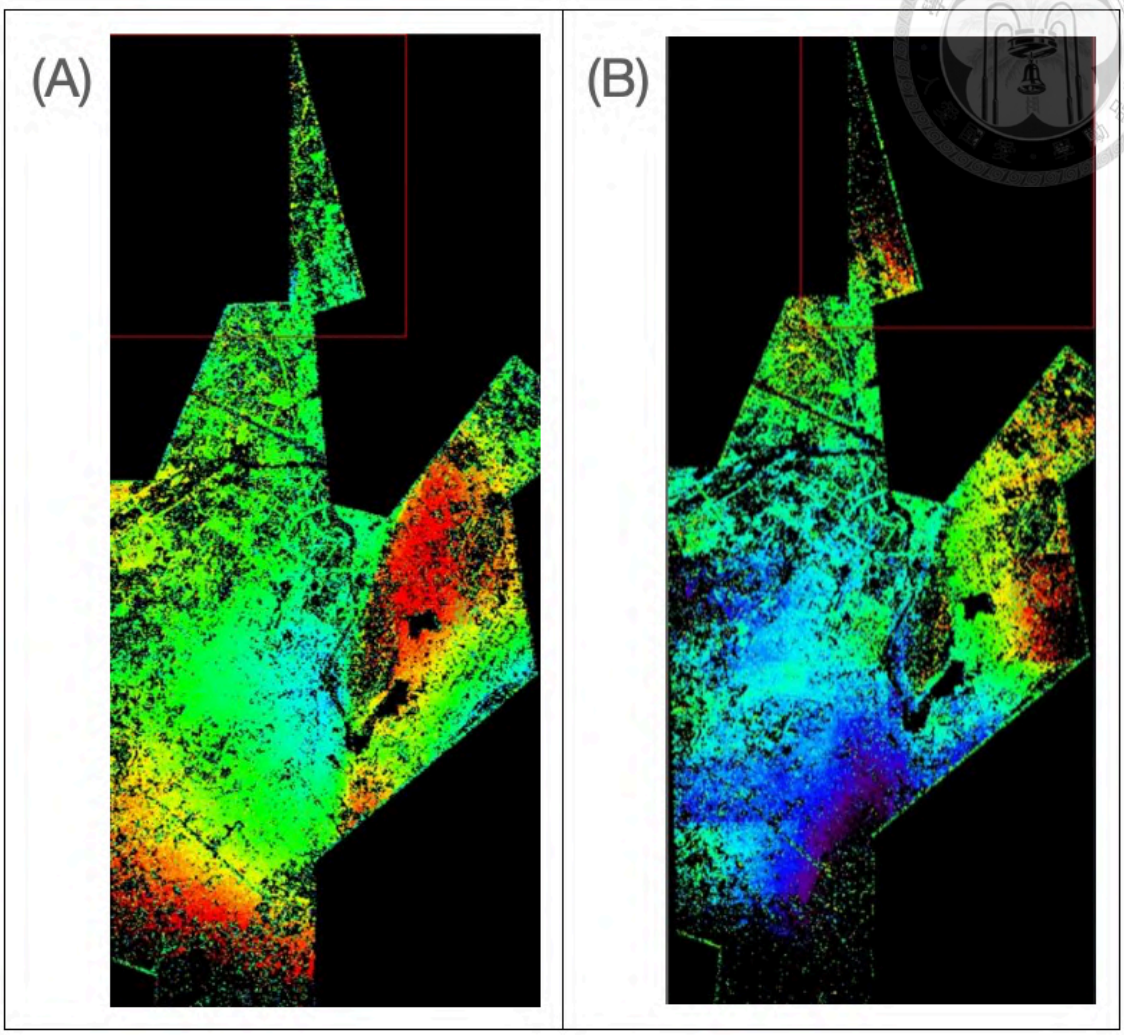

Fig. 9. Initial COSI-Corr results. To make our COSI-Corr results visible, we adjusted the ENVI color tables to rainbow-black and set the interactive stretching between -1 to 1. Red indicates pixels moving north and east; blue indicates pixels moving south and west; green means no movement on that pixel. (A) COSI-Corr pixel offset with 128*128 pixels window size snd 32 pixels step in N-S direction. (B) COSI-Corr pixel offset with 128*128 pixels window size snd 32 pixels step in E-W direction.

3.2.1.3 GNSS correction

Since COSI-Corr only interpreted the pattern of movement and might contain systematic error, we need to constrain it with GNSS data. For GNSS correction, we calculated the difference between GNSS and image displacement, averaged over a radius of 250 m from the GNSS point, and performed Inverse Distance Weighting (IDW) interpolation to obtain a GNSS difference surface (Fig. 10).

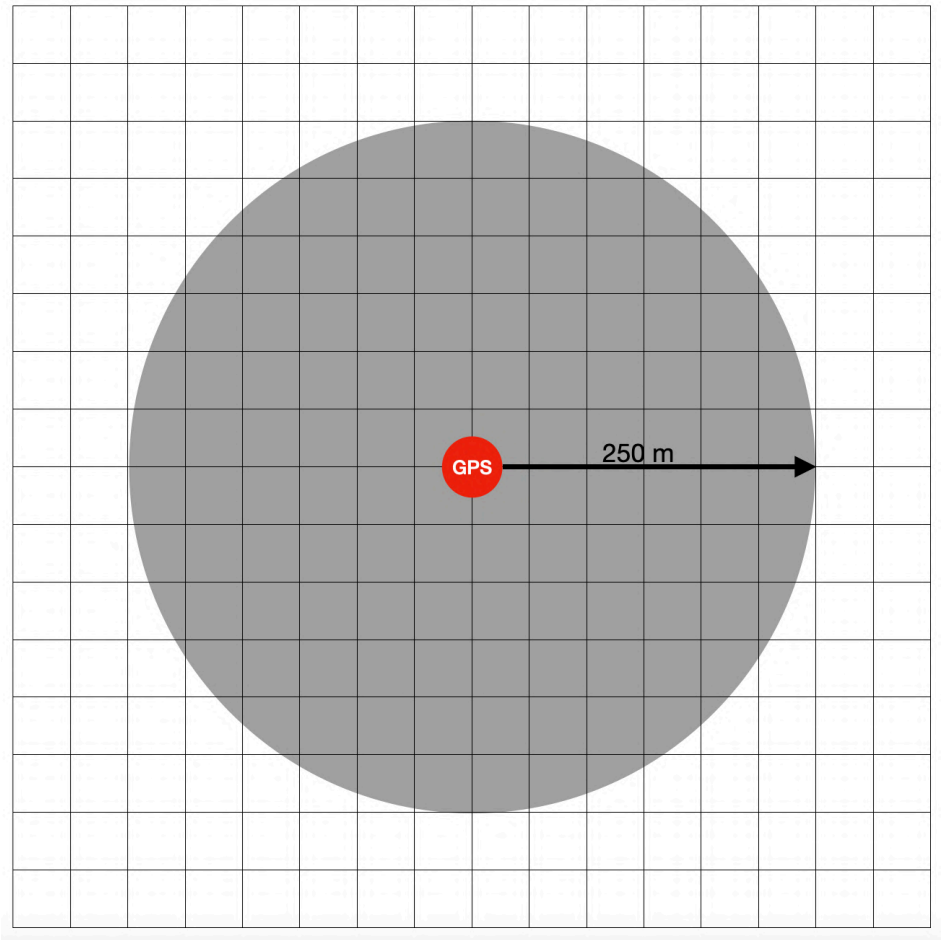

Fig. 10. Averaged pixel shift values within 250 m radius of the GPS point. The actual GNSS location might not be exactly at the center of a pixel or at a junction, and the search range is the principal point of each pixel that is covered within a 250 m radius.

The Continuous GPS (cGPS) and campaign GPS data were from Yen et al. (2019) (Table 4). cGPS data were gathered by the CWB, Central Geological Survey, Institute of Earth Sciences of Sinica Academia, Industrial Technology Research Institute, and ETEC, and provided by the ETEC. Coseismic deformation from cGPS is the difference between the 7-day average before earthquake and 5-day average after the earthquake for most of the cGPS sites. For the sites affected by the 4 February 2018 earthquake, coseismic deformation was the position differences between two days before the 6 February main event and seven days after the earthquake. Campaign GPS data were the difference between May 2017 and February 2018. Before conducting any interpolation, we removed the extreme values of offset, which should be smaller than 1 meter in any direction. Finally, we fit the displacement field to the GPS difference surface to calculate the final calibrated displacement field.

Station	Longitude (°)	Latitude (°)	TWD97 X	TWD97 Y	Cos_N (mm)	Cos_E (mm)
B345	121.628	23.9988	313895.1792	2655032.6771	457.88	504.9
BP05	121.6059	24.017	311637.9083	2657038.5050	-288.99	-41.45
BP06	121.604	24.0166	311444.8075	2656993.3737	-286.77	-40.52
HG01	121.6316	23.9992	314261.2686	2655078.6154	375.81	542.65
HGC9	121.6128	23.9902	312352.7741	2654073.4045	437.33	103.04
HUAL	121.6135	23.9754	312431.1355	2652434.5970	431.35	164.2
ML03	121.6163	23.9811	312713.3175	2653067.1212	520.31	314.4
ML14	121.6087	23.9858	311937.6908	2653584.2911	-303.08	14.25
MS05	121.6107	23.9851	312141.5400	2653507.6457	18.15	37.85
ND06	121.6208	24.0086	313157.8195	2656114.7953	503.15	393.76
NDH1	121.5956	23.9624	310615.6267	2650987.0272	-311.55	29.04
NDH5	121.6181	24.01	312882.4440	2656268.6392	146.73	58.92

Table 4. List of Global Positioning System (GPS) coseismic deformation data used in this research.

However, the number of GNSS stations is far from enough and they were unevenly distributed. The GNSS correction field is strongly affected by the algorithm we chose, shown in Fig. 11.

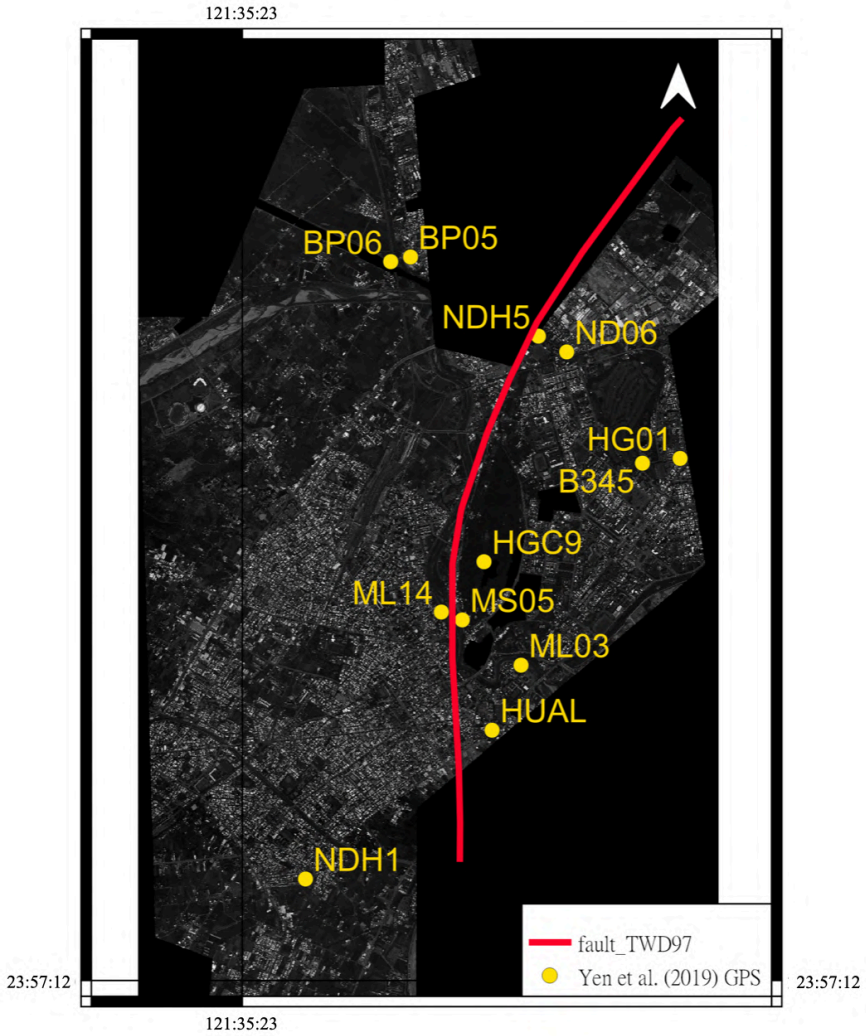

Fig. 11. Map of GNSS locations.

3.2.1.4 3D displacements by comparing 3D models

Since the SfM technique can generate 3D models before and after the earthquake, this study compared the 3D models to estimate vertical displacements as well. We subtracted the DSM before the earthquake from the one after the earthquake and got the vertical changes from this event.

3.2.2 Comparison with other geodetic data

One way to evaluate our displacement field is to compare our result with other geodetic data. We used the Pleiades COSI-Corr result from Kuo et al. (2019) to compare sub-pixel correlation results. We divided the correction process into two steps. To minimize the effect from extreme values and noises, we first resample both results into bigger pixels, 500*500 meters. Then we calculated the difference between them and interpolated the difference into original resolution, 9.6*9.6 meters. Step 2 is to subtract the displacement difference field from our original COSI-Corr displacement field, shown in Fig.12. In addition, we also compared the result with InSAR-derived coseismic displacements from Lin (2022).

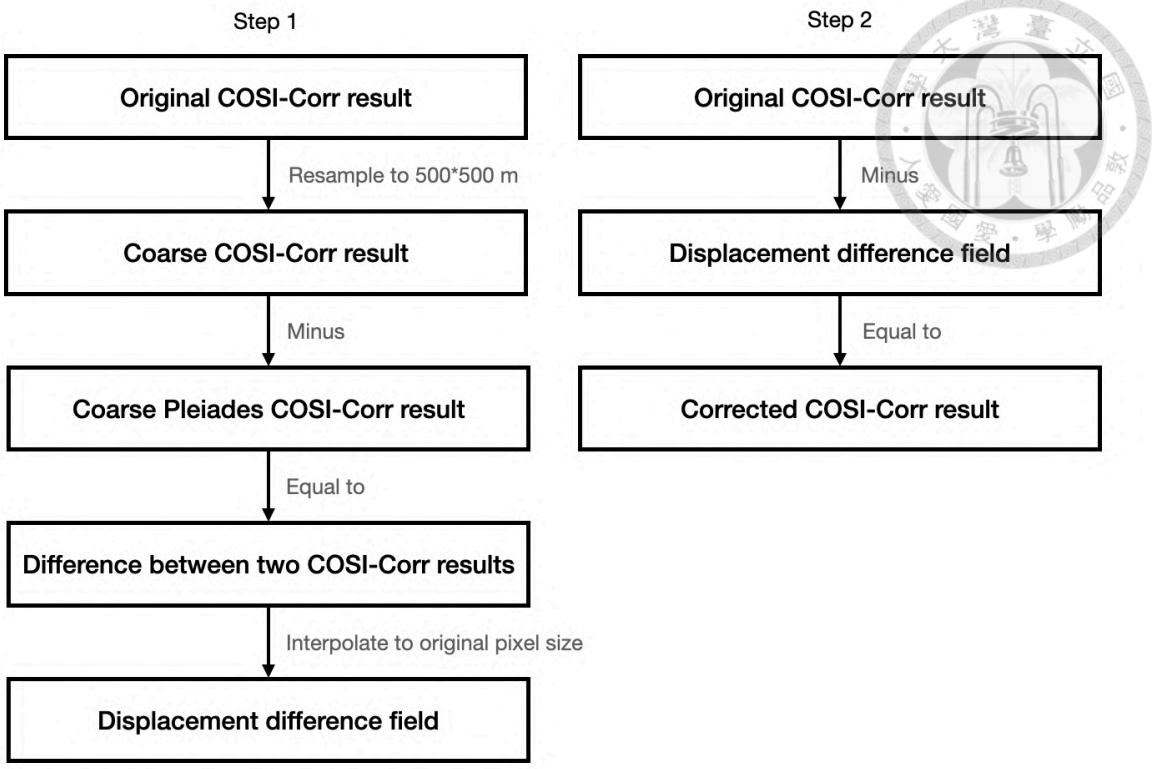

Fig. 12. Flow chart of COSI-Corr correction with the result from Kuo et al. (2019).

3.2.3 Estimation of off-fault deformation

This research calculated the percentage of the off-fault deformation with the by fitting many displacement profiles to quantify the along-strike variations of the off-fault deformation following the methods of Zinke et al. (2014) and Milliner et al. (2015). Once the amount of percentage of the off-fault deformation for each profile along the strike is computed, the along-strike variation was visualized by a variation map.

Chapter 4 Results

4.1 Displacement field

4.1.1 N-S displacement field

The N-S displacement field shows a clear pattern of left-lateral strike-slip fault. The hanging wall moved 95 centimeters to the north; the foot wall moved 45 centimeters to the south. Close to Ji'an Township there was also northward movement, which we speculate that this is because adjacency. As for the airport, according to field investigation, there were fault scarps all the way to Chihsingtan Beach. We suggest if the aerial image of the airport were available, the offset in the airport should be consistent with the foot wall (Fig. 13).

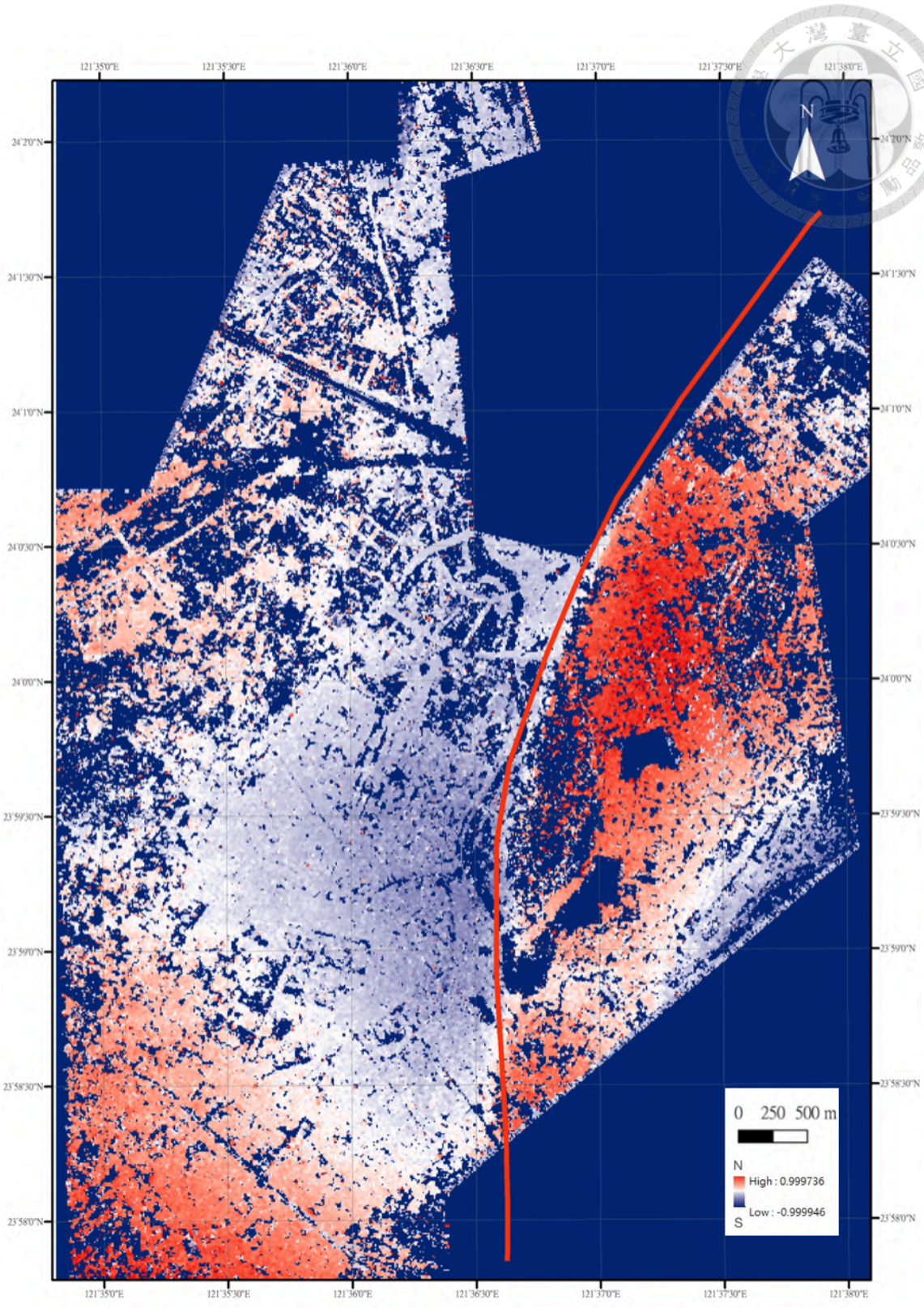

Fig. 13. COSI-Corr displacement field in N-S direction. The hanging wall moved 90-100 centimeters to the north; the foot wall moved 40-50 centimeters to the south.

4.1.2 E-W displacement field

The E-W displacement field shows the hanging wall moved toward the east by one meter, but only the side close the sea, suggesting that the hanging wall rotated during the earthquake. The foot wall also moved by 30 cm to the west. The E-W direction displacement field indicates great amount of off-fault deformation. It is clear in the field that the main deformation is not on the fault line, especially in the southern part. The furthest deformation is more than 1 kilometer away from the fault line (Fig. 14).

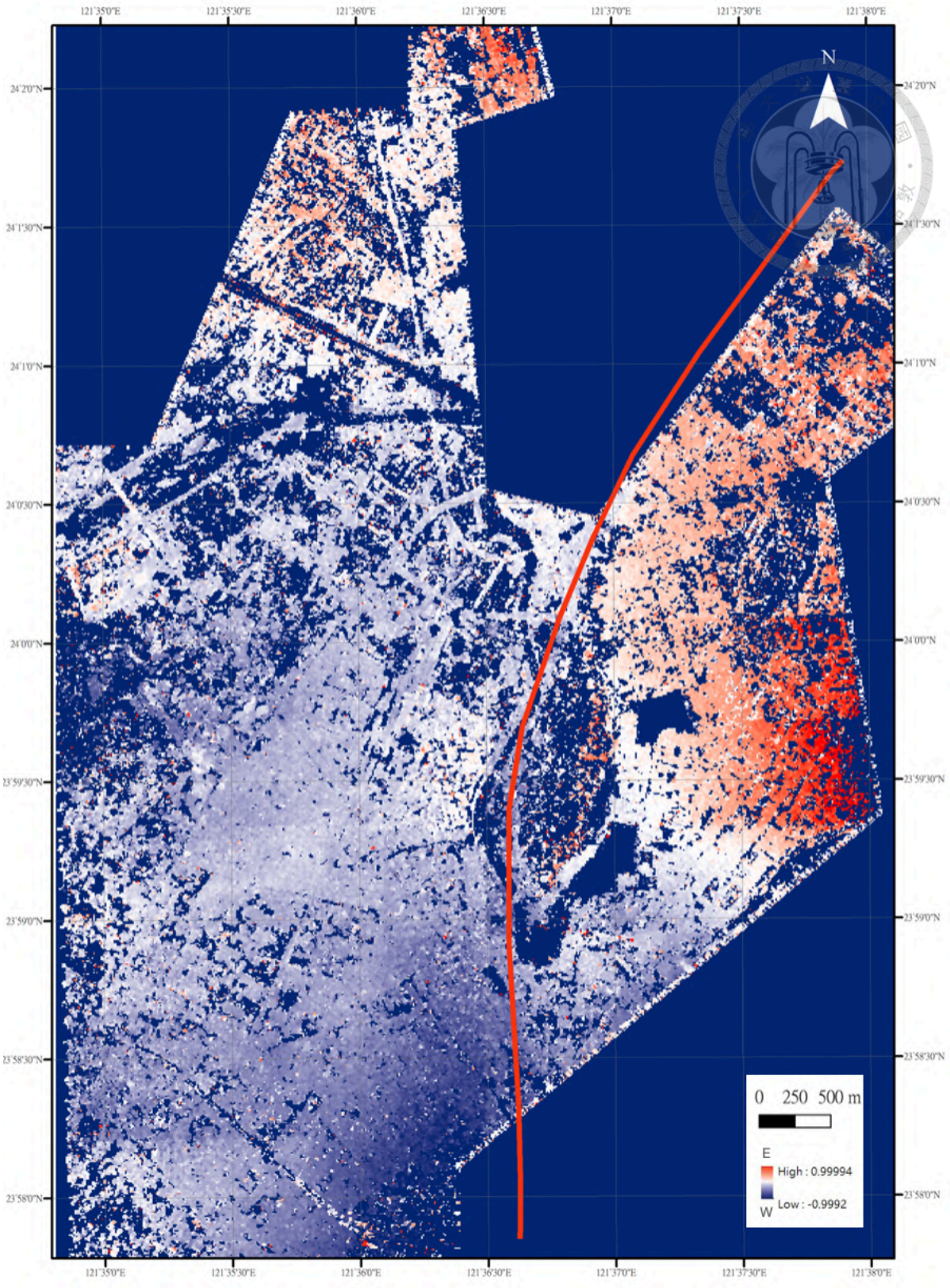

Fig. 14. COSI-Corr displacement field in E-W direction.

4.1.3 Vertical displacement field

The DSM subtraction before and after the 2018 earthquake revealed the vertical change, which was close to zero. The reason could come from the original aerial photos not having enough transverse and longitudinal overlap. Without enough overlap, the we had less angles to make the models three-dimensional. Therefore, the result is basically 2-D and presents no vertical difference. This outcome could also come from the lack of 5-meter DEM in Hualien area. We used the 20-meter DEM instead and added the elevation from the 2010A version of ground control points from National Land Surveying and Mapping Center. Due to low DEM resolution and uneven GNSS distribution, the overall altitude was not well constructed. All in all, the deformation in this earthquake is basically horizontal. No vertical displacement is a result that matches reality (Fig. 15).

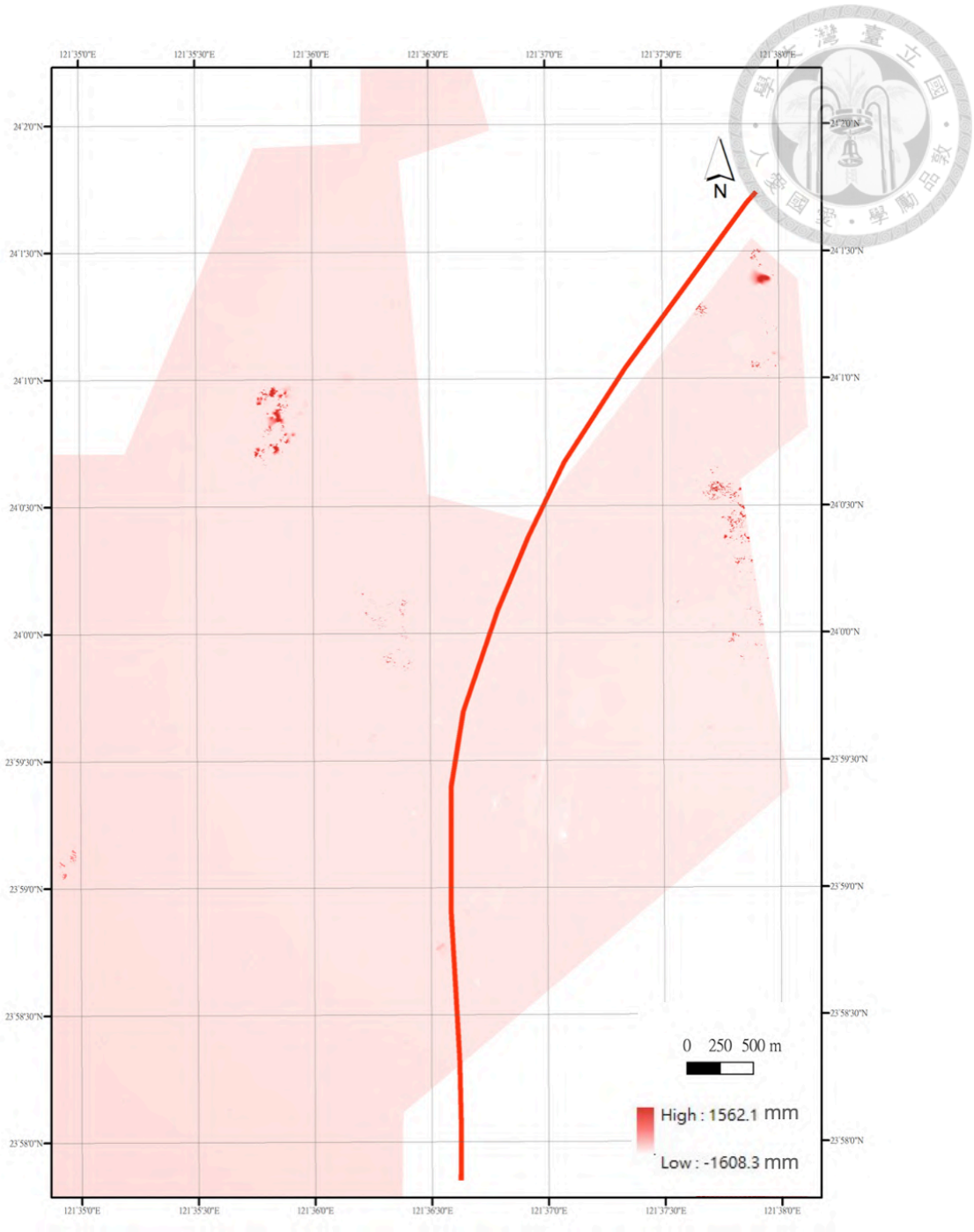

Fig. 15. DSM subtraction before and after the earthquake. Light pink area means there is no difference between the two DSMs.

4.1.4 GNSS-corrected displacement field

Surface displacement in GNSS corrected COSI-Corr shows the same pattern of movement in both directions. We found the best correction method is the one with Kriging interpolation, based on how well it merged with the COSI-Corr displacement field from Pleiades images. Green dots are GNSS stations from Yen (2019).

4.1.4.1 GNSS-correction with IDW interpolation

COSI-Corr displacement corrected with IDW interpolation is mainly consistent with the trend we saw in Pleiades COSI-Corr, except for the slight northward movement in Ji'an Township (Figs. 16 and 17).

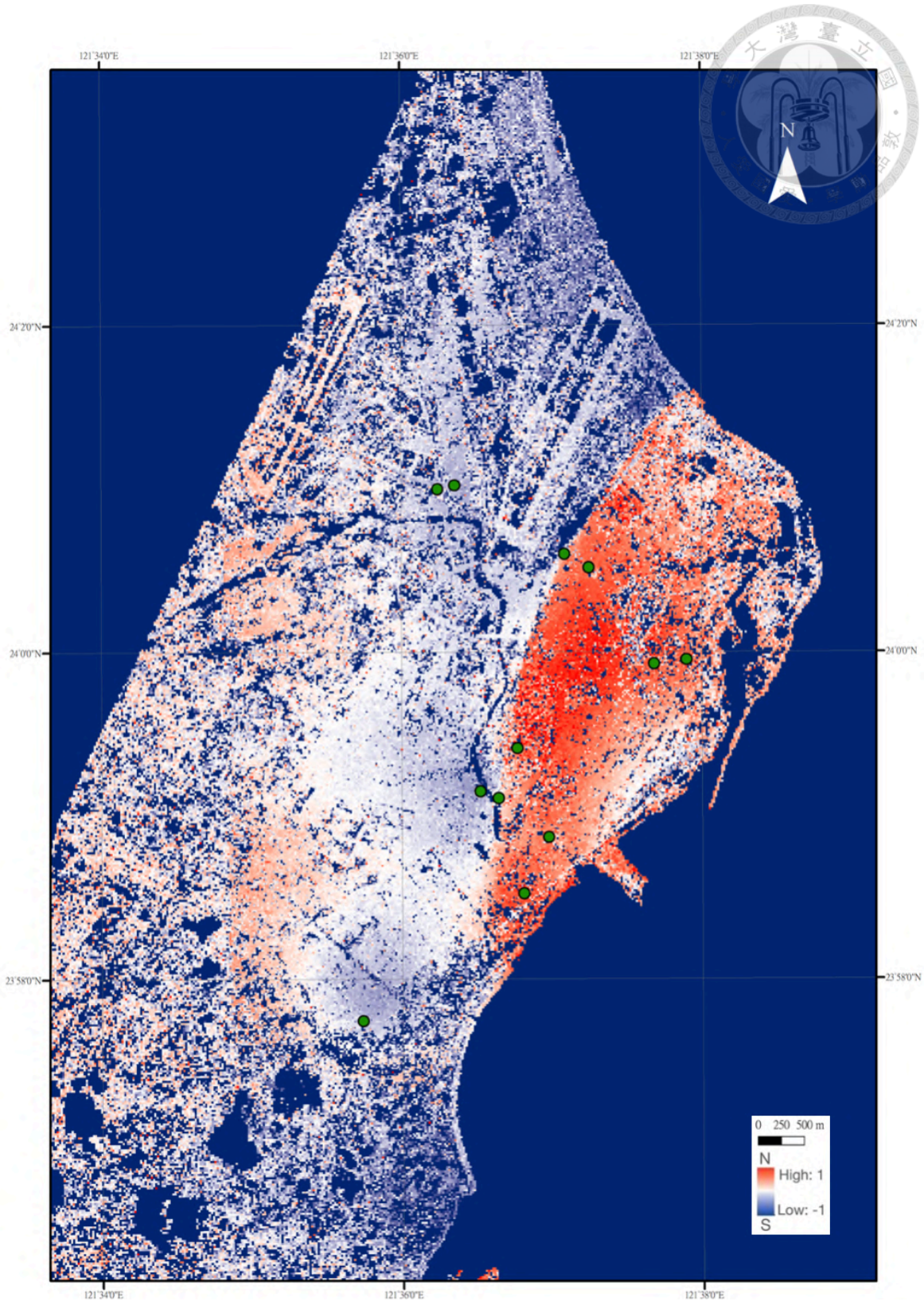

Fig. 16. COSI-Corr GNSS-corrected displacement field with IDW in N-S direction.

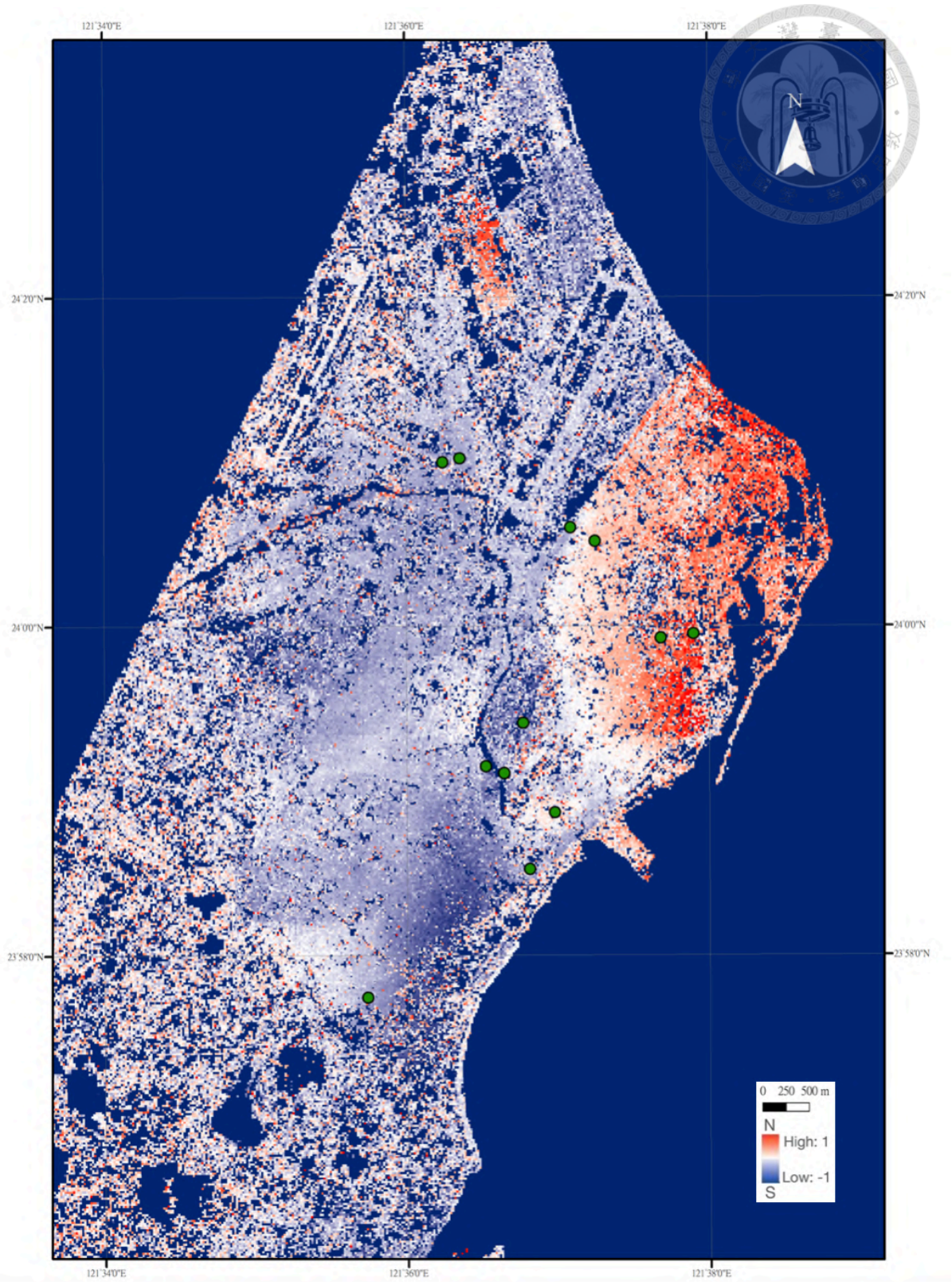

Fig. 17. COSI-Corr GNSS-corrected displacement field with IDW in E-W direction.

4.1.4.2 GNSS-correction with Kriging interpolation

Displacement field with Kriging interpolation is the one most consistent with the COSI-Corr displacement field from Pleiades images. The pixel offset is extremely similar to the one of Pleiades imagery but with better resolution in both directions (Figs. 18 and 19).

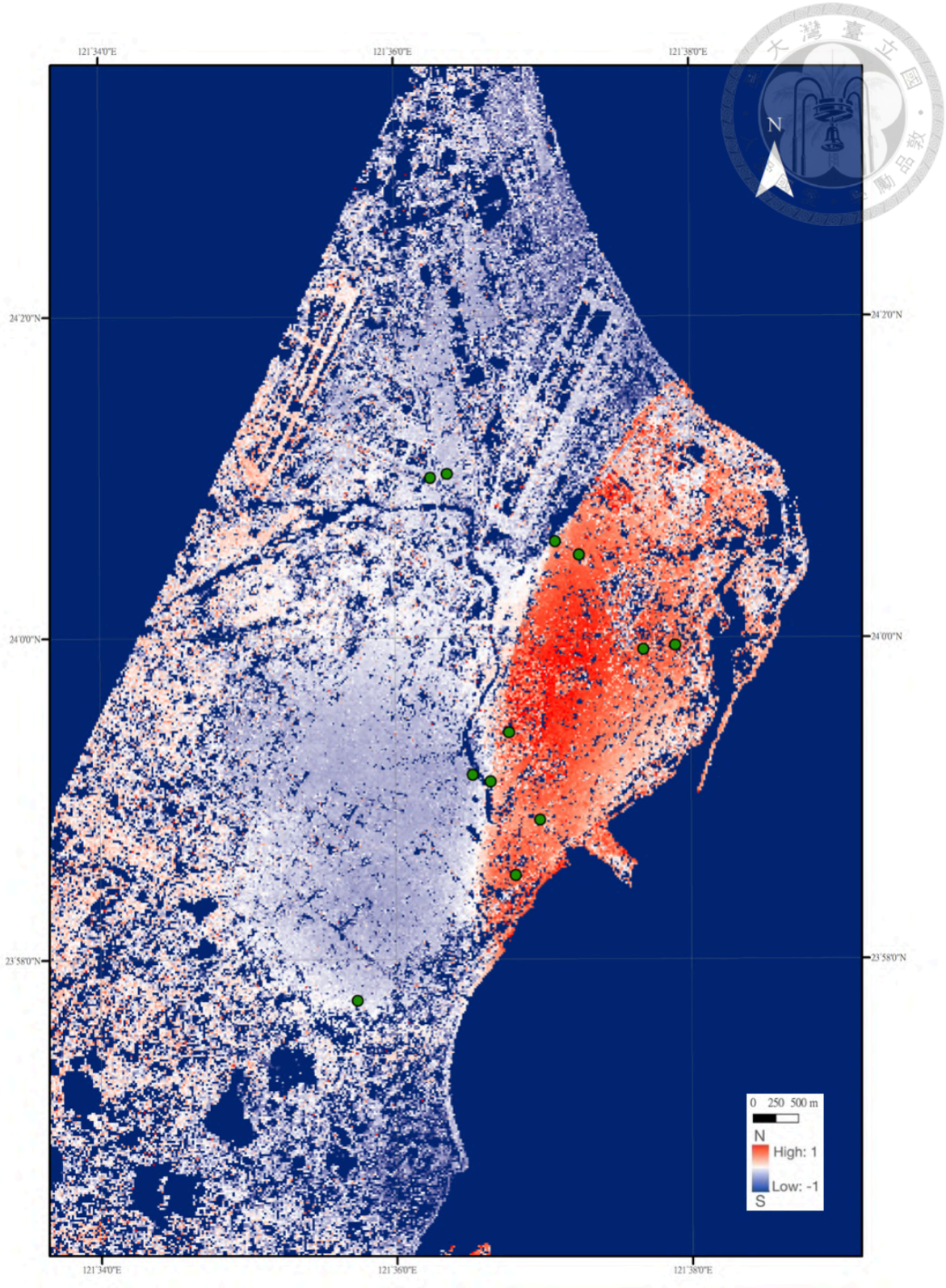

Fig. 18. COSI-Corr GNSS-corrected displacement field with Kriging in N-S direction.

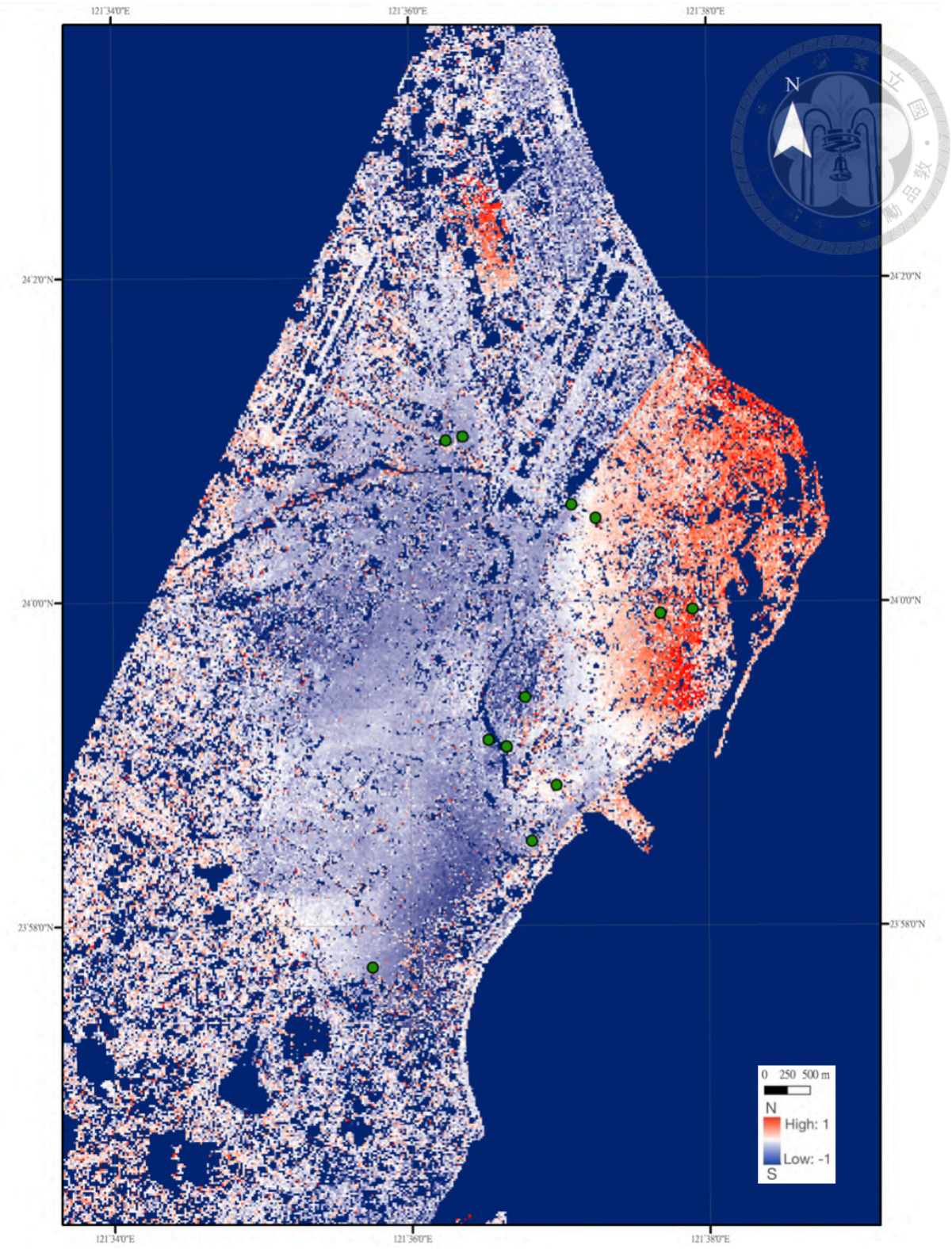

Fig. 19. COSI-Corr GNSS-corrected displacement field with Kriging in E-W direction.

4.1.4.3 COSI-Corr-corrected displacement field

Displacement field corrected with Pleiades COSI-Corr is probably the worst among all corrections. The offset of the hanging wall is strongly enhanced, and the incorrect offset trend on Ji'an Township is even more significant in N-S direction. As for in E-W direction, the offset on both blocks turned patchy and was inconsistent with field investigation (Figs. 20 and 21).

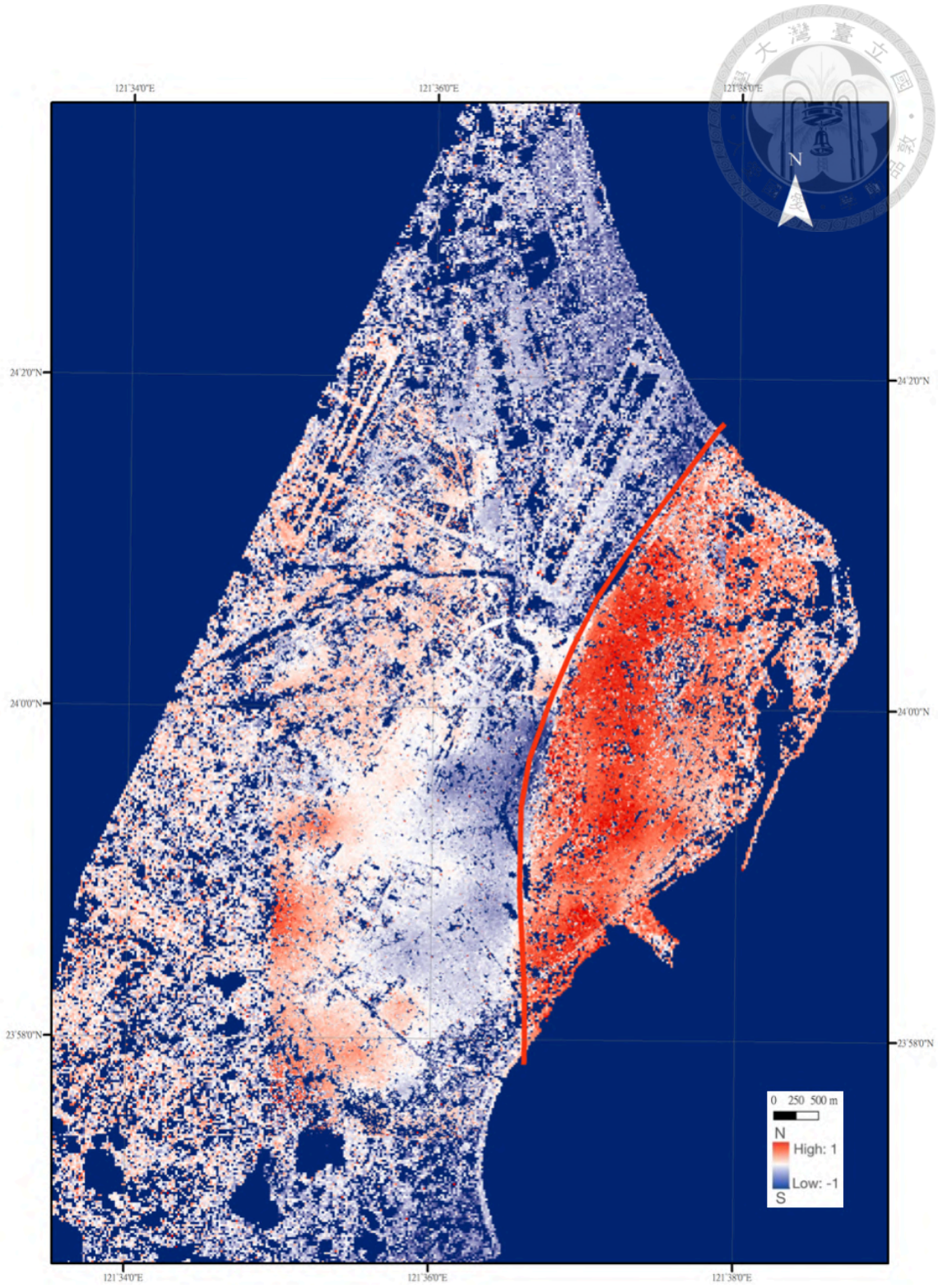

Fig. 20. COSI-Corr corrected displacement field in N-S direction.

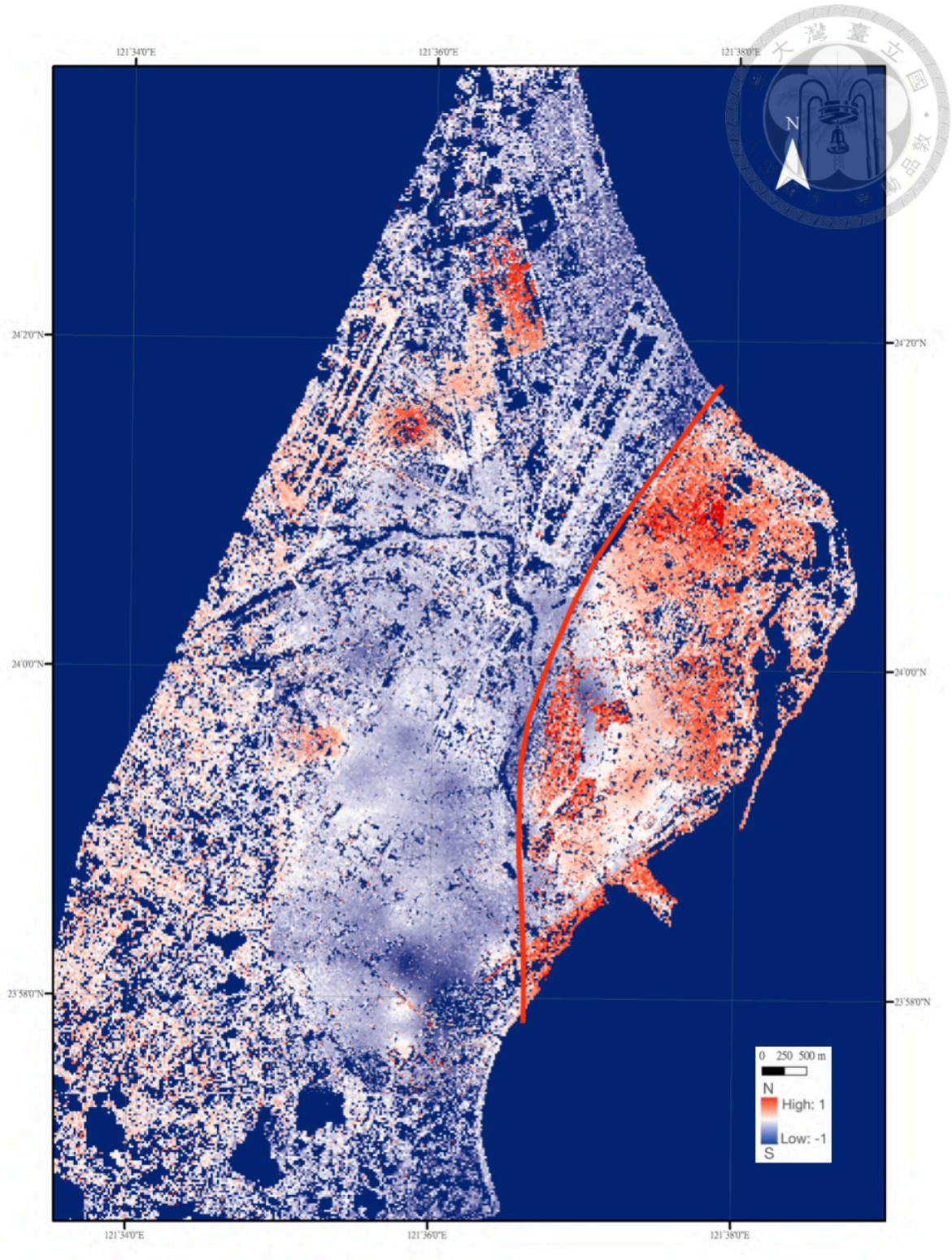

Fig. 21. COSI-Corr corrected displacement field in E-W direction.

4.2 Along-strike variation

4.2.1 Along strike profiles

We placed 19 profiles along the field-investigated fault line by Shyu et al. (2020) in the N-S direction COSI-Corr result and observed two patterns separately from the middle and the southern part. The length of the profiles is 600 meters, and the distance between them is 200 meters. In the middle part, the offset difference is very clear, reaching 0.85 meter maximum. From profile 8, the offset difference decreases but still has upward trend to the east (Fig. 22).

We drew another fault line based on the displacement field and profile results in green. The fault line drawn based on N-S displacement field is shifted to the east by 41 to 206 meters from the fault line by Shyu et al. (2020).

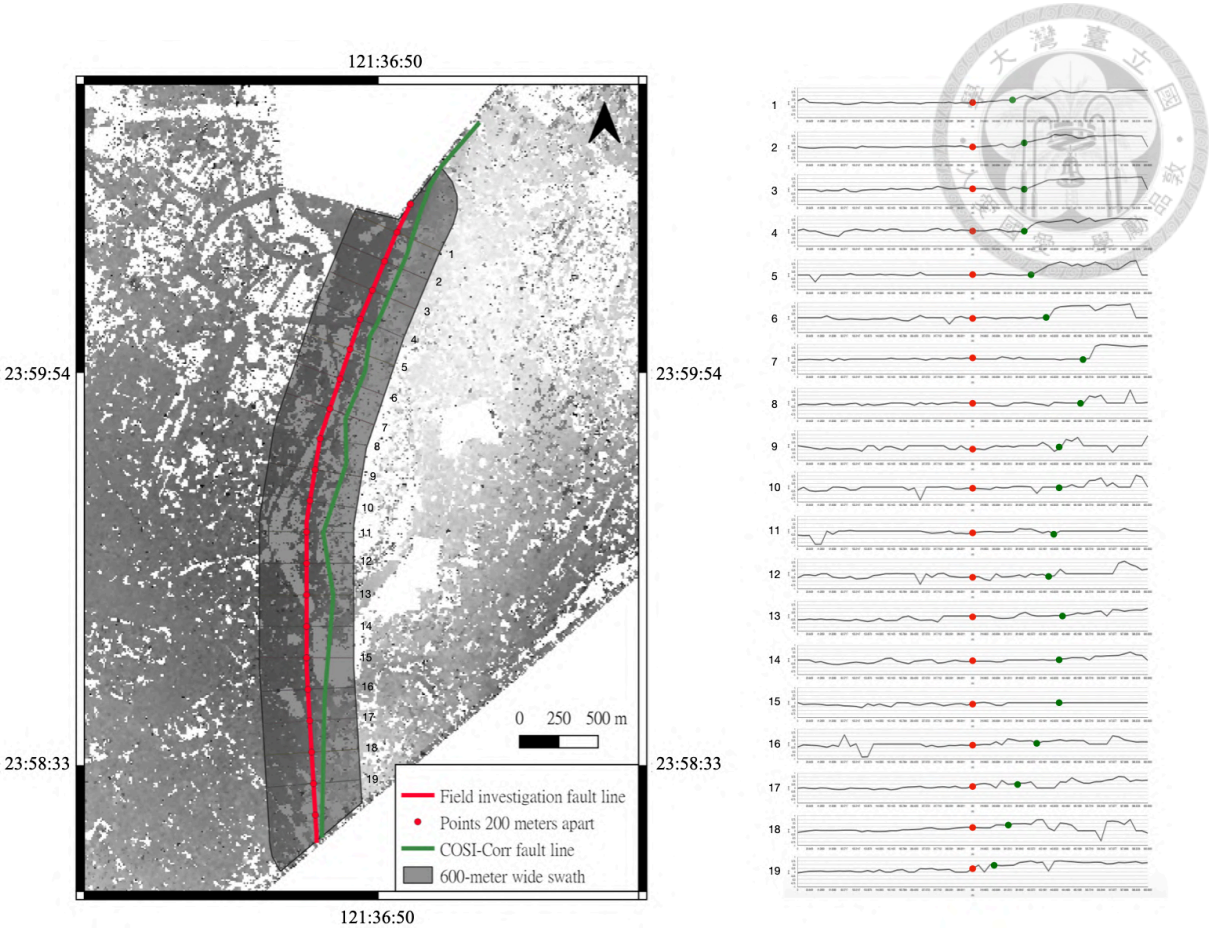

Fig. 22. Nineteen along strike profiles. The red line is the fault line by Shyu et al. (2020). Profiles are 200 meters apart from each other, and their centers are marked with red dots. The green line is the fault line based on N-S displacement field, marked with green dots on the profiles.

However, as we placed the detailed field investigation by Huang et al. (2019), we noticed that the surface ruptures actually fitted better with our fault line from correlation displacement field, especially in the middle section (Fig. 23). We then calculated the percentage of off-fault deformation along the fault by subtracting the on-fault displacement from the total displacement, and found that the off-fault percentage in the middle section was relatively low but increasing toward the south (Fig. 24).

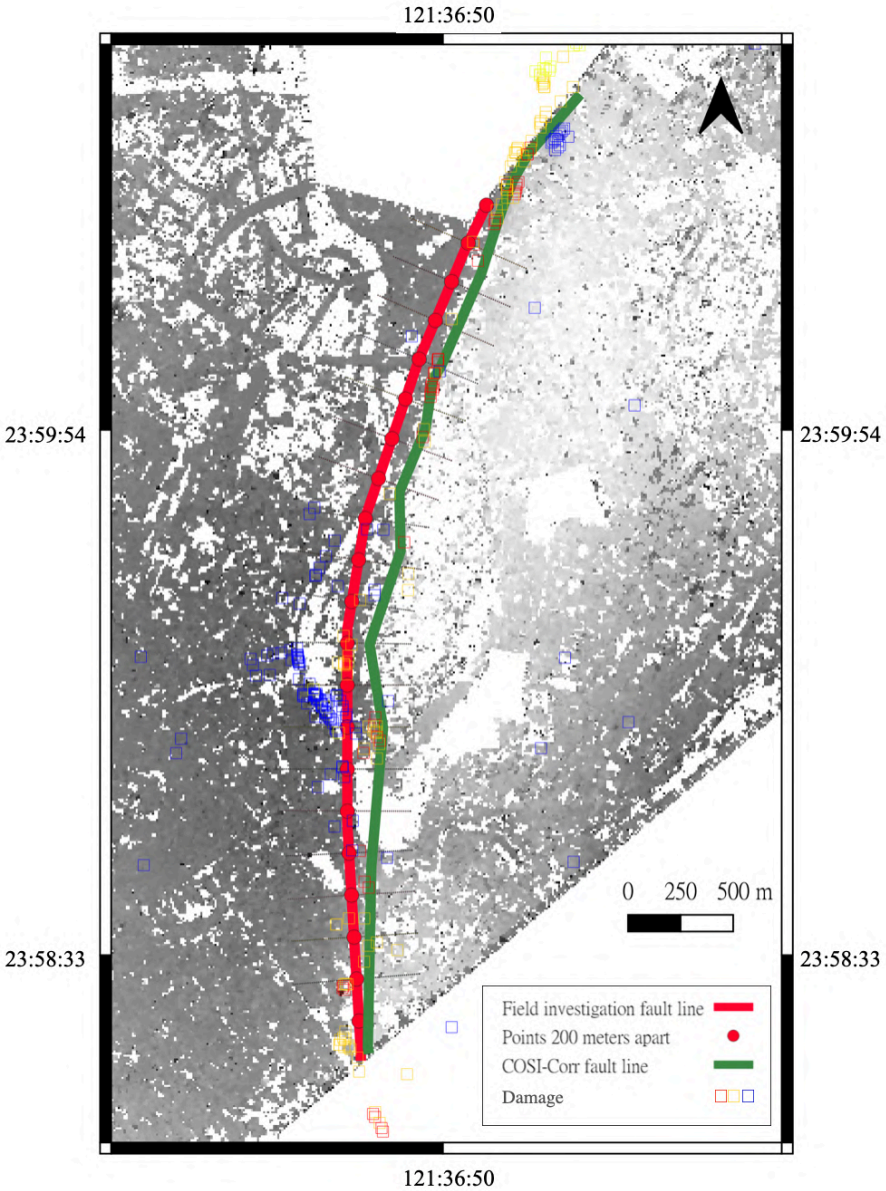

Fig. 23. Map of damage and ruptures investigated by Huang et al. (2019).

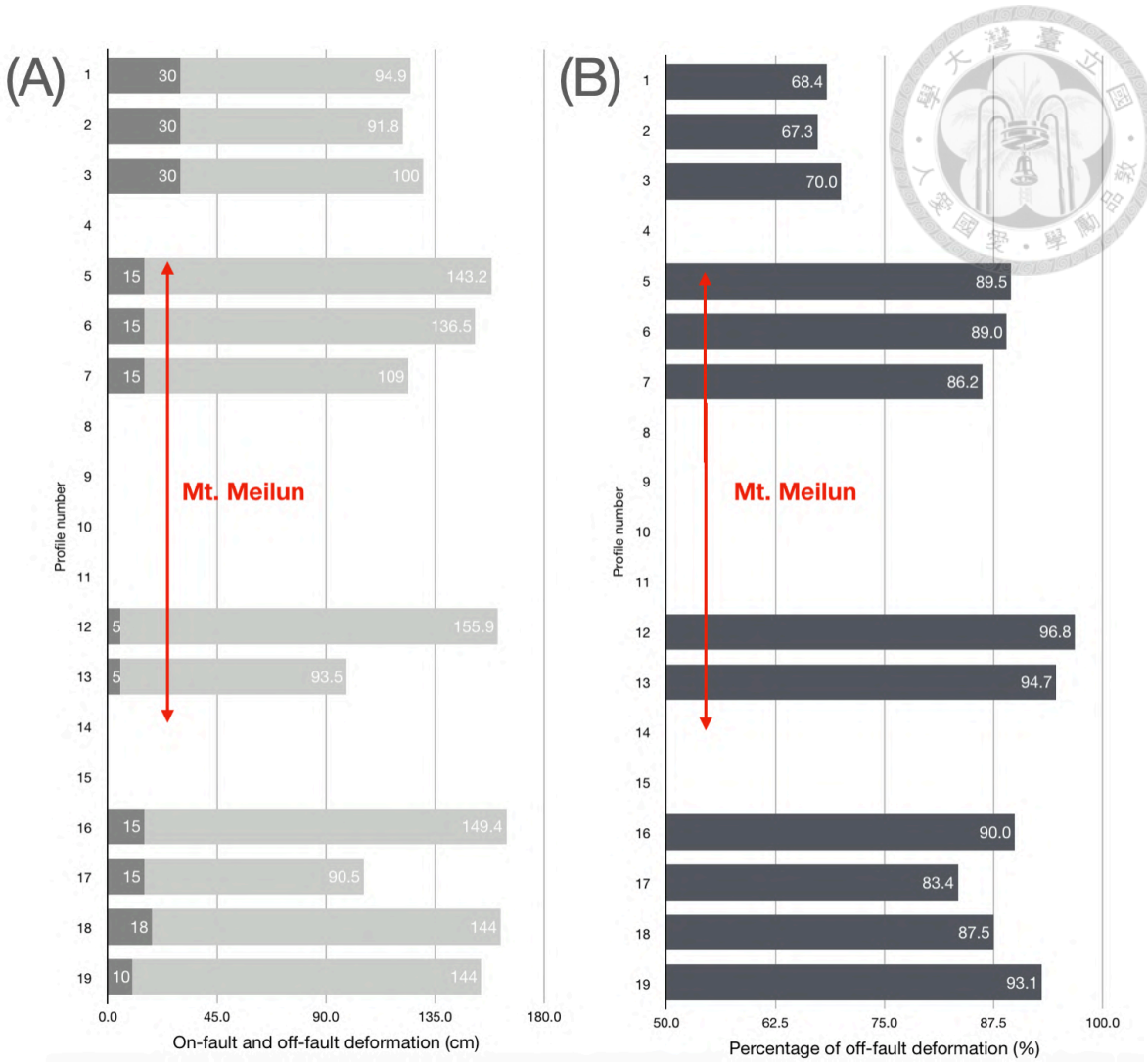

Fig. 24 Along-strike off-fault deformation. (A) On-fault and off-fault deformation. (B) Percentage of off-fault deformation.

More, we compared our profiles with profiles with displacement fields of Pleiades' COSI-Corr and InSAR (Fig. 25). The profiles were longer (1000 m) this time due to the density of pixels in InSAR.

Fig. 25. Profiles of (A) aerial images COSI-Corr, (B) Pleiades COSI-Corr and (C) InSAR from north to south. (D) Overlapping of aerial images COSI-Corr Pleiades COSI-Corr profiles.

4.2.2 Results from InSAR

We compared our displacement field with the results from InSAR displacement by Lin (2022). Lin corrected his displacement field of with DInSAR+MAI+POT correction (Figs. 26 and 27). We subtracted the Lin's InSAR result from our COSI-Corr and found no systematic error in the city, where the ruptures locate (Fig. 28). The coastline had lower pixel offset value, which we believe came from the high cloud coverage of original aerial photos. The maximum displacement between two walls in N-S direction is 80 centimeters, which is significantly lower than our maximum 140 centimeters displacement. InSAR coseismic displacement field provides ground changes in the airport and the cloud-covered coast, and therefore makes us better understand the relative motion of two tectonic plates.

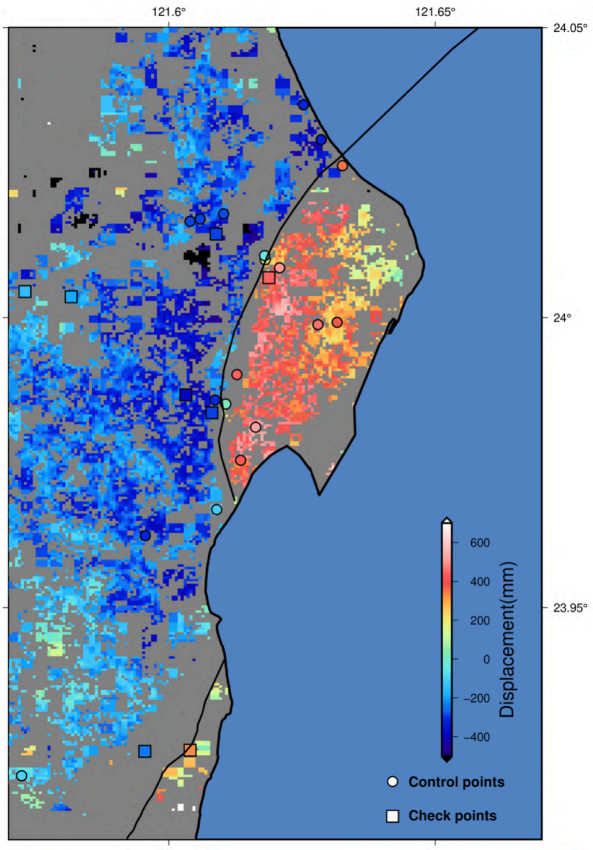

Fig. 26. Corrected displacement field of DInSAR+MAI+POT in N-S direction.

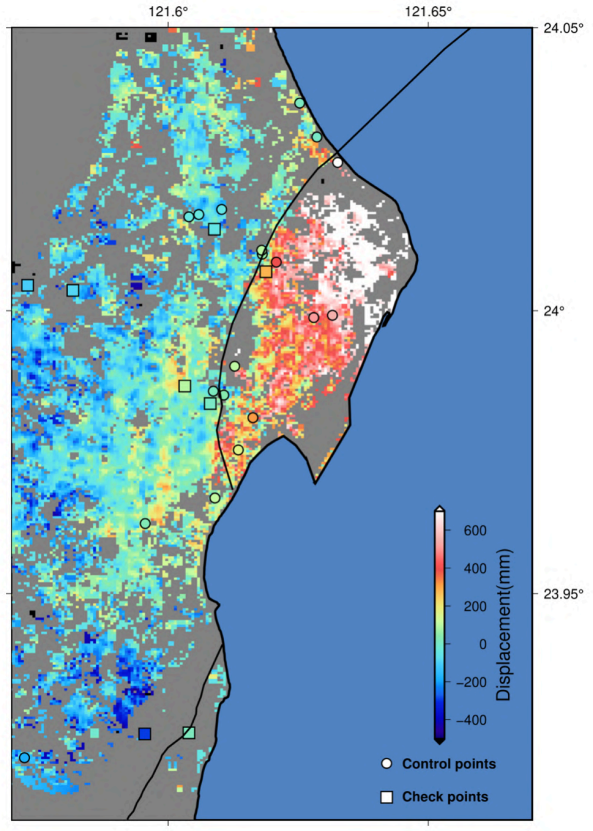

Fig. 27. Corrected displacement field of DInSAR+MAI+POT in E-W direction. (Lin, 2022)

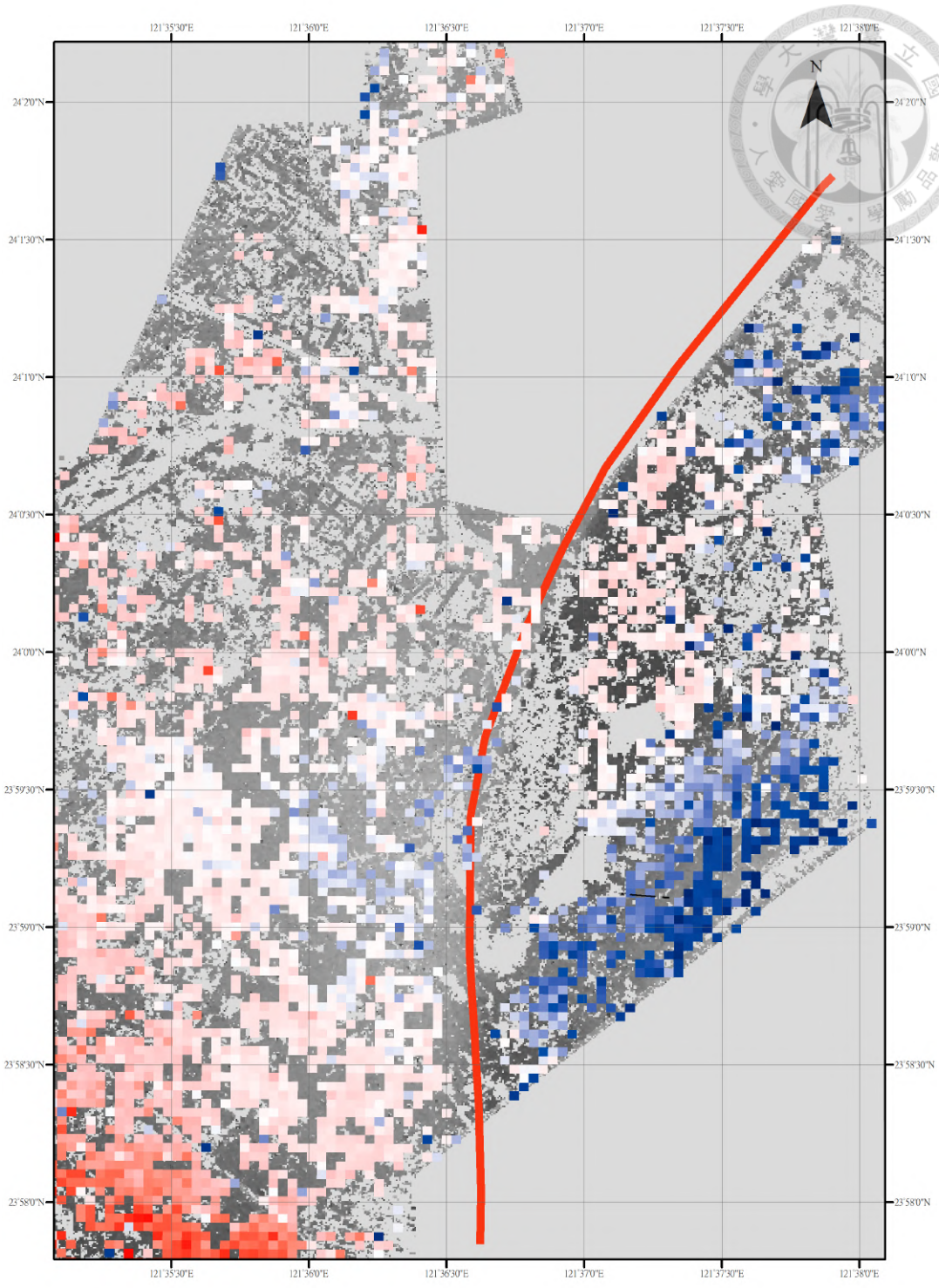

Fig. 28. COSI-Corr and InSAR subtraction in N-S direction. Blue pixels are places where COSI-Corr pixel offset is smaller than the offset value from InSAR, the red ones are the opposite.

Chapter 5 Discussion

5.1 Fine and detailed coseismic displacement field

With the high-resolution aerial images, we defined a clear fault line consistent with the detailed field investigation by Huang et al. (2019) and Lin et al. (2019). The displacements across the hanging and foot walls is also defined, and it allows us to better understand the relative movement of the two blocks. We found our displacement field had similar trends and values from overlapping with Pleiades' profile with higher resolution. Our COSI-Corr resolution is finer by 3 times than the one of Pleiades imagery COSI-Corr and by more than 30 times of the one of InSAR. It is also shown in the profiles, helping us to capture precise, complicated movement in the near field.

5.2 Along-strike variation off-fault deformation

The width difference between the field investigation and optical correlation displacements may indicate a large component of off-fault deformation. Off-fault deformation occurred along the middle and southern part of the Milun fault. As for the northern-middle section, there is no obvious deformation far way from the fault line. Field observation showed that the measurable cumulative left-lateral offset across the rupture zone is generally less than 30 cm (except for the maximum 77 cm offset in the northern section). However, our image correlation results indicate a higher left-lateral displacement of 91-156 cm, which is generally well localized in the north, and relatively distributed in the south (over a zone of 300 m around the main rupture). The percentage of off-fault deformation, relatively low (~68%) in the middle section but increasing

toward the south (~97%), also indicates the same pattern. We suggest that more than ~68% of the deformation may have occurred off-fault during the 2018 earthquake.

The 68-97% off-fault deformation estimated in the Hualien earthquake is larger than the ~46% and ~39% off-fault deformation reported during the 1992 Landers and 1999 Hector Mine earthquakes (Milliner et al., 2015), and the 2013 Balochistan earthquake (Zinke et al., 2014).

5.3 Explanation for off-fault variation

This large percentage of off-fault deformation may indicate the Milun fault is structurally immature and unable to localize deformation onto a structurally simple fault in Meilun River's alluvial fan. According to Milliner et al. (2015), this could come from the less consolidated geologic units (e.g., young alluvial sediments), like those in the southern section of Milun fault. This geological condition may result from high precipitation and sedimentation rates in east Taiwan. Unlike interior Southern California and western Balochistan, Taiwan has the climate that leads to the development of thicker and weaker water-rich sediments at the surface, which may decrease slip localization (Kuo et al., 2019). Along the southern part of the Milun fault, electric resistivity analysis across the area that later ruptured in 2018 suggested that at least the top ~120 m of sediment is composed of young alluvium deposits (Chien, 2015). These weaker alluvial deposits are less capable of localizing coseismic deformation (e.g., Zinke et al., 2014) and consequently may result in a higher ratio of off-fault deformation.

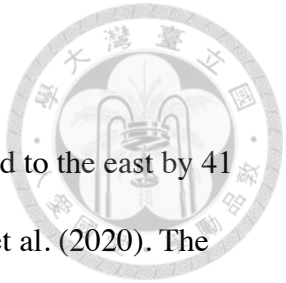

5.4 Exact fault trace

The fault line drawn based on N-S displacement field is shifted to the east by 41 to 206 meters compared to the originally-mapped fault line by Shyu et al. (2020). The maximum width of the fault line zone is 315 meters and the minimum is less than 10 meters in N-S direction.

5.5 Conclusion

We successfully applied high-resolution aerial images to study the 3D deformation field produced by the 2018 Hualien earthquake. The results reveal a spectacular left-lateral rupture along the Milun fault, with almost no vertical motion. The deformation pattern suggests the northern to middle section of the Milun fault formed a narrow and localized zone of surface deformation, which becomes much wider and more distributed along the southern half of the fault.

Comparison of field survey data with our near-field image correlation results indicates 68-97% of the deformation may have occurred off-fault, especially along the southern half of the Milun fault where the zone of distributed deformation can be as wide as 300 m. The zone of off-fault deformation could be explained by the physical properties of the soft, young alluvial sediments overlying the Milun fault.

References

- Barnhart, W. D., Gold, R. D., and Hollingsworth, J. (2020). Localized fault-zone dilatancy and surface inelasticity of the 2019 Ridgecrest earthquakes. Nature Geoscience, 13, 699–704. https://doi.org/10.1038/s41561-020-0628-8

- Bonilla, M. G. (1975). A review of recently active faults in Taiwan. U.S. Geological Survey Open-File Report 75- 41, Version 1.1, Reston, VA, 42 pp. http://geopubs.wr.usgs.gov/open-file/of75-41/

- Bonilla, M. G. (1977). Summary of Quaternary faulting and elevation changes in Taiwan. Memoir of the Geological Society of China, 2, 43-55.

- Chen, C. W., and Zebker, H. A. (2002). Phase unwrapping for large SAR interferograms: Statistical segmentation and generalized network models, Institute of Electrical and Electronics Engineers Transactions on Geoscience and Remote Sensing. 40, 1709–1719.

- Chen, C.-Y., Lee, J.-C., Chen, Y.-G., and Chen, R.-F. (2014). Campaigned GPS on Present-day crustal deformation in northernmost Longitudinal Valley preliminary results, Hualien Taiwan. Terrestrial, Atmospheric and Oceanic Sciences, 25, 337-357, doi: 10.3319/TAO.2013.12.25.01(TT). http://tao.cgu.org.tw/index.php/articles/archive/geology/item/1215

- Cheng, S.-N., Yeh, Y. T., Hsu, M.-T., and Shin, T.-C. (1999). Photo Album of Ten Disastrous Earthquakes in Taiwan, Central Weather Bureau, 290 pp.

- Chien, L. K. (2015). An Electric Resistivity Study of the Faults in the Taitung Longitudinal Valley, National Central University, Eastern Taiwan.
- Dominguez, S., Avouac, J., and Michel, R. (2003), Horizontal coseismic deformation of the 1999 Chi-Chi earthquake measured from SPOT satellite images: Implications for the seismic cycle along the western foothills of central Taiwan, Journal of Geophysical Research, 108, B2, 2083, https://doi.org/10.1029/2001JB000951
- Hsu, T. L. (1962). A study on the coastal geomorphology of Taiwan, Proceedings of the Geological Society of China 5, 29–45.
- Hsu, Y. C., Chang, C. P., Yen, J. Y., Kuo-Chen, H., and Wang, C. C. (2019). Investigating the structure of the Milun Fault from surface ruptures of the 2018 Hualien earthquake. Terrestrial, Atmospheric and Oceanic Sciences, 30(3), 337-350. https://10.3319/TAO.2018.09.28.01
- Huang, M. H., and Huang, H. H. (2018). The complexity of the 2018 Mw 6.4 Hualien earthquake in East Taiwan. Geophysical Research Letters, 45(24), 13,249-13,257. https://doi.org/10.1029/2018GL080821
- Huang, S. Y., Yen, J. Y., Wu, B. L., Yen, I. C., and Chuang, R. Y. (2019). Investigating the Milun fault: The coseismic surface rupture zone of the 2018 Hualien earthquake, Taiwan, Terrestrial, Atmospheric and Oceanic Sciences., 30, 311-355. https://doi.org/10.3319/TAO.2018.12.09.03
- Kuo, Y. T., Wang, Y., Hollingsworth, J., Huang, S. Y., Chuang, R. Y., Lu, C. H., Hsu, Y. C., Tung, H., Yen, J. Y., and Chang, C. P. (2019). Shallow Fault Rupture of the Milun Fault in the 2018 Mw 6.4 Hualien Earthquake: A High-Resolution Approach

from Optical Correlation of Pléiades Satellite Imagery. Seismological Research Letters, 90(1), 97-107. https://doi.org/10.1785/0220180227

- Kuo-Chen, H., Wu, F. T., and Roecker, S. W. (2019). Aftershock sequence of the 2018 Mw 6.4 Hualien earthquake in eastern Taiwan from a dense seismic array data set. Seismological Research Letters. 90(1), 60-67. https://doi.org/10.1785/0220180233.

- Lee, S. J., Lin, T. C., Liu, T. Y., and Wong, T. P. (2019). Fault-to-fault jumping rupture of the 2018 Mw 6.4 Hualien earthquake in eastern Taiwan. Seismological Research Letters, 90(1), 30-39. https://doi.org/10.1785/0220180182.

- Lin, L. C. (2022). Derivation of 3D Coseismic Displacement Field from Different SAR Algorithms – Case Study of the 2018 Hualien Earthquake.

- Lin, Y. S., Chuang, R. Y., Yen, J. Y., Chen, Y. C., Kuo, Y. T., Wu, B. L., Huang, S. Y., and Yang, C. J. (2019). Mapping surface breakages of the 2018 Hualien earthquake by using UAS photogrammetry. Terrestrial, Atmospheric and Oceanic Sciences, 30(3), 1-16. https://doi.org/10.3319/TAO.2018.12.09.02

- Lin, M.-S. and Hsiao, C.-L. (1998). Strike-Slip Tectonics in the Milun Conglomerate Terrace. Eastern Taiwan Studies, 3, 13-29, doi: 10.6275/JETS.3.13-29.1998. (in Chinese) https://www.airitilibrary.com/Publication/alDetailedMesh?DocID=a0000573-199812-201005100082-201005100082-13-29

- Milliner, C. W. D., Dolan, J. F., Hollingsworth, J., Leprince, S., Ayoub, F., and Sammis, C. G. (2015). Quantifying near-field and off-fault deformation patterns of the 1992 Mw 7.3 Landers earthquake, Geochemistry, Geophysics, Geosystems, 16, 1577–1598. https://doi.org/10.1002/2014GC005693

- Sandwell, D. T., Mellors, R., Tong, X., Wei, M., and Wessel, P. (2011). GMTSAR: An InSAR Processing System Based on Generic Mapping Tools: Manual, 1 pp.

- Shyu, J. B. H., Chen, C. F., and Wu, Y. M. (2016). Seismotectonic characteristics of the northernmost Longitudinal Valley, eastern Taiwan: Structural development of a vanishing suture. Tectonophysics, 692, 295-308. https://doi.org/10.1016/j.tecto.2015.12.026

- Shyu, J. B. H., Sieh, K., and Chen, Y. G. (2005). Neotectonic architecture of Taiwan and its implications for future large earthquakes. Journal of Geophysical Research, 110(B8), B08402. https://doi.org/10.1029/2004JB003251

- Shyu, J. B. H., Yin, Y. H., Chen, C. H., Chuang, Y. R., and Liu, S. C. (2020). Updates to the on-land seismogenic structure source database by the Taiwan Earthquake Model (TEM) project for seismic hazard analysis of Taiwan, Terr. Atmos. Ocean. Sci., 31, 469-478, doi: 10.3319/TAO.2020.06.08.01

- Van Puymbroeck, N., Michel, R., Binet, R., Avouac, J, and Taboury, J. (2000). Measuring earthquakes from optical satellite images. Applied Optics, **39**, 3486-3494. https://opg.optica.org/ao/viewmedia.cfm?uri=ao-39-20-3486&seq=0

- Wang, C. (2005). A modeling study of the response of tropical deep convection to the increase of cloud condensational nuclei concentration: 1. Dynamics and microphysics. Journal of Geophysical Research: Atmospheres, 110, D21211. https://doi.org/10.1029/2004JD005720

- Wu, B. L., Yen, J. Y., Huang, S. Y., Kuo,, Y. T., and Chang, W. Y. (2019). Surface deformation of 0206 Hualien earthquake revealed by the integrated network of RTK

GPS. Terrestrial, Atmospheric and Oceanic Sciences, 30(3), 301-310. https://doi.org/10.3319/TAO.2019.05.27.01

- Yang, Y.-C. (1953). Earthquakes in Hualien in the latest 41 years. Hualien Literatures, 1, 67-71. (in Chinese)

- Yang, Y.-H., Hu, J.-C., Tung, H., Tsai, M.-C. Q., Chen, Q. Xu, Zhang, Y.-J., Zhao, J.-J., Liu, G.-X., Xiong, J.-N., Wang, J.-Y., Yu, B., Chiu, C.-Y., and Su, Z., (2018). Co-Seismic and Postseismic Fault Models of the 2018 Mw 6.4 Hualien Earthquake Occurred in the Junction of Collision and Subduction Boundaries Offshore Eastern Taiwan. Remote Sensing, 10, 1372, doi: 10.3390/ rs10091372. https://www.mdpi.com/2072-4292/10/9/1372

- Yen, J. Y., Lu, C. H., Chang, C. P., Hooper, A. J., Chang, Y. H., Liang, W.-T., Chang, T.-Y., Lin, M.-S. ,and Chen, K.- S. (2011). Investigating active deformation in the northern Longitudinal Valley and City of Hualien in eastern Taiwan using persistent scatterer and small-baseline SAR interferometry. Terrestrial, Atmospheric and Oceanic Sciences, 22, 291-304. https://doi.org/10.3319/TAO.2010.10.25.01(TT)

- Yen, J.-Y., Lu, C.-H., Dorsey, R. J., Kuo-Chen, H., Chang, C.-P., Wang, C.-C., Chuang, R. Y., Kuo, Y.-T., Chiu, C.-Y., Chang, Y.-H., Bovenga, F., and Chang, W.-Y. (2019). Insights into seismogenic deformation during the 2018 Hualien, Taiwan, earthquake sequence from InSAR, GPS, and modeling. Seismological Research Letters, 90, 78-87. https://doi.org/10.1785/0220180228

- Zinke, R., Hollingsworth, J., and Dolan, J. F. (2014), Surface slip and off-fault deformation patterns in the 2013 MW 7.7 Balochistan, Pakistan earthquake:

Implications for controls on the distribution of near-surface coseismic slip, Geochemistry, Geophysics, Geosystems, 15, 5034–5050. https://doi.org/10.1002/2014GC005538